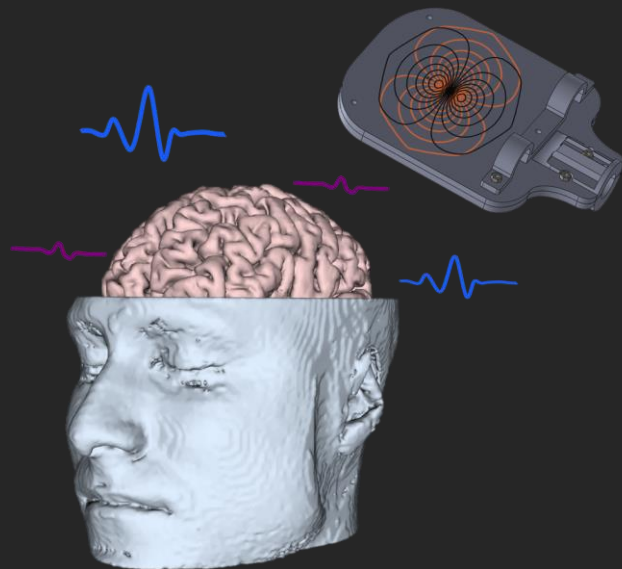


UNIVERSIDADE DE SÃO PAULO  
FFCLRP – DEPARTAMENTO DE FÍSICA

VICTOR HUGO DE OLIVEIRA E SOUZA

**Development of instrumentation for neuronavigation and  
transcranial magnetic stimulation**

**Desenvolvimento de instrumentação para neuronavegação  
e estimulação magnética transcraniana**



RIBEIRÃO PRETO – SP

2018

UNIVERSIDADE DE SÃO PAULO  
FFCLRP – DEPARTAMENTO DE FÍSICA  
PROGRAMA DE PÓS-GRADUAÇÃO EM FÍSICA APLICADA À  
MEDICINA E BIOLOGIA

**Development of instrumentation for neuronavigation and  
transcranial magnetic stimulation**

**Desenvolvimento de instrumentação para neuronavegação  
e estimulação magnética transcraniana**

Victor Hugo de Oliveira e Souza

Versão Corrigida

(Versão original encontra-se na unidade que aloja o  
Programa de Pós-graduação)

Tese apresentada à Faculdade de Filosofia, Ciências e  
Letras de Ribeirão Preto da USP, como parte das  
exigências para obtenção do título de Doutor em  
Ciências. Área: Física Aplicada à Medicina e Biologia.

Orientador: Prof. Dr. Oswaldo Baffa Filho

**RIBEIRÃO PRETO – SP**

**2018**

Autorizo a reprodução e divulgação total ou parcial deste trabalho, por qualquer meio convencional ou eletrônico, para fins de estudo e pesquisa, desde que citada a fonte.

## FICHA CATALOGRÁFICA

Souza, Victor Hugo de Oliveira e

Desenvolvimento de instrumentação para neuronavegação e estimulação magnética transcraniana / Victor Hugo de Oliveira e Souza; orientador Oswaldo Baffa Filho. Ribeirão Preto – SP, 2018.

74 f.: il.

Tese (Doutorado em Ciências) – Programa de Pós-graduação em Física Aplicada à Medicina e Biologia, Faculdade de Filosofia, Ciências e Letras de Ribeirão Preto, Universidade de São Paulo, 2018.

Orientador: Prof. Dr. Oswaldo Baffa Filho

Versão corrigida

1. Neuronavegação. 2. Estimulação magnética transcraniana. 3. Planejamento cirúrgico. 4. Potencial evocado motor. 5. Orientação da bobina. 6. Impressão 3D.

**Ao meu pai Alcione, minha mãe Irani  
e minha irmã Lud!**

# Acknowledgments

A cada dia fica mais evidente para mim que trabalhar em conjunto com pessoas de bem e compartilhar experiências fazem com que as tarefas cotidianas sejam mais prazerosas. Durante o desenvolvimento deste trabalho evoluí pessoalmente e adquiri uma experiência profissional que moldaram minha percepção da vida. Um grande número de pessoas compõe uma rede que, direta e indiretamente, contribuíram significativamente para que esta tese pudesse ser concretizada. A estas pessoas, gostaria de expressar minha sincera gratidão.

Prof. Oswaldo Baffa agradeço pela confiança, conselhos e amizade nestes últimos dez anos. Durante a iniciação científica, mestrado e doutorado sua orientação foram de extrema importância para minha formação, espero ter sido capaz de absorver apenas uma pequena fatia de tanta experiência positiva que me foi passada. Sua sabedoria aliada à humildade e carisma o destacam como um líder diferenciado e admirável.

No Laboratório de Biomagnetismo, iniciei uma jornada a convite do meu “irmão mais velho” Prof. André Peres. Poder seguir os projetos que você iniciou e aprender a trabalhar com um grande amigo foi uma honra para mim. Sou muito grato pela sua paciência e amizade em me ensinar e mostrar as belezas da carreira científica, mesmo quando a dúvida aparecia. Prof. Marco Garcia, a você muito obrigado por apoiar minhas ideias e me ensinar com muita tranquilidade a enxergar a conexão entre o instrumental e o biológico. Tem sido uma enorme satisfação poder trabalhar contigo. Caro Renan Matsuda, obrigado por ser meu braço direito e esquerdo. Esta tese tem muito do seu esforço e só pude chegar até aqui graças à sua dedicação nos nossos projetos. Obrigado pela amizade e companheirismo de todo dia.

Agradeço aos meus amigos Leonardo Rakauskas, Felipe Grillo, Thiago Moraes, Paulo Amorim, Vitor Cuziol, Anderson Apunike e Dr. Carlo Rondinoni, foi muito bom trabalhar com vocês. Também agradeço à oportunidade de trabalhar com o Prof. Antonio Carneiro, Prof. Hélio Machado, Prof. Theo Pavan, Prof<sup>a</sup>. Claudia Vargas, Prof<sup>a</sup>. Adriana Conforto, Prof. Dráulio Araújo, Prof. Carlos Garrido e Dr. Jorge Silva. Do Departamento de Física, agradeço ao Fernando Torrieri, Matheus Silveira, Lourenço Rocha, Gabriela Tardelli, Guilherme Turato, Fabrício Simozo e Leonardo França por um ambiente de trabalho agradável e de muito bom humor. Aos funcionários, Nilza Marino e Ricardo Santos por auxiliar nos assuntos administrativos, e aos funcionários Carlos Silva, Lourenço Rocha e Élcio Navas pelo auxílio técnico para execução dos experimentos.

My stay in Espoo, Finland, made it possible to get along with fantastic people. Thanks to Prof. Risto Ilmoniemi who welcomed me into his group and guided me during the internship. I feel honored to be able to work with such a brilliant and charismatic person. Thanks to Dr. Jaakko Nieminen, Dr. Lari Koponen, and Sergei Tugin, for the fellowship and shared experiences during our joint project, I learned a lot from you. Thanks Dr. Jyrki Mäkelä and Dr. Juha Montonen for the assistance during the experiments in BioMag Laboratory. I also would like to thank the remaining NBE members for their friendship and good times during my stay, especially Dr. Tuomas Mutanen, Niko Mäkelä and Ivan Zubarev. Thank you, Dr. Julio Hernandez-Pavon for the friendship and warm welcome in Finland. Thanks also to the guys from the group Lasagna for your friendship.

Em Ribeirão Preto, a coisa se complica um pouco. Foram 11 intensos anos com uma rede de amigos que eu precisaria de um livro dedicado para poder citar cada um. Vocês tiveram uma contribuição inestimável na minha formação como pessoa e trouxeram tantos bons momentos que foi difícil desvincular desse ambiente. Em especial à Rep. Tosca, onde morei desde 2007 e convivi com as melhores pessoas que poderia desejar. Aos companheiros da Rep. Gruta pela amizade, ao time de handebol da Filô e da LAURP pelos momentos de descontração. À XXIX de Fevereiro, pelas magníficas discussões, festas e risadas.

Aos meus amigos de Patrocínio, com quem cresci e pude compartilhar as primeiras experiências de vida. Uma dessas experiências foi a despedida do amigo *in memoriam* Renato Almeida, com quem aprendi bastante sobre como viver a vida intensamente, e a quem gostaria especialmente de agradecer pela amizade.

Nestes últimos cinco anos, a minha parceira Alessandra Vairo me incentivou com muito amor e carinho, estando lado a lado ou à distância. Sou muito feliz por poder compartilhar tantas experiências boas com você e te ter em meu dia a dia.

Ao meu pai Alcione e minha mãe Irani, que me proporcionaram uma educação com princípios de bem, me deram liberdade para trilhar meu caminho e são minhas referências para tudo. À minha irmã Ludmila que esteve sempre ao meu lado quando precisava. Estar com vocês é não precisar de mais nada. Agradeço também à minha grande e estimada família.

Por fim, agradeço ao apoio financeiro dado pelo Conselho Nacional de Desenvolvimento Científico e Tecnológico (CNPq processo: 140787/2014-3), Erasmus Mundus SMART<sup>2</sup> (Referência: 552042-EM-1-2014-1-FR-ERA MUNDUSEMA2) e Coordenação de Aperfeiçoamento de Pessoal de Nível Superior (CAPES).

**“Por que não?”**

# Resumo

**SOUZA, VHO. Desenvolvimento de instrumentação para neuronavegação e estimulação magnética transcraniana.** 2018. 74 f. Tese (Doutorado) – Faculdade de Filosofia, Ciências e Letras de Ribeirão Preto, Universidade de São Paulo, Ribeirão Preto, 2018.

A neuronavegação e a estimulação magnética transcraniana (EMT ou TMS, do termo em inglês *transcranial magnetic stimulation*) têm sido apresentadas como ferramentas valiosas em aplicações clínicas e de pesquisa. A neuronavegação possibilita a localização de instrumentos em relação a imagens anatômicas durante procedimentos de intervenção neurológica. Por sua vez, a EMT permite o estudo não invasivo da função cerebral e o tratamento de doenças neurológicas. Apesar da importância de ambas as técnicas, o alto custo dos sistemas de neuronavegação e a reduzida precisão espacial da EMT em ativar estruturas cerebrais limitam suas aplicações. Sendo assim, o objetivo desta tese foi: i) desenvolver um software de neuronavegação gratuito e de código aberto, ii) estudar a combinação entre neuronavegação e impressão 3D para planejamento cirúrgico, e iii) construir uma bobina de EMT multicanal com controle eletrônico da orientação do campo elétrico (CE). Na primeira parte, desenvolvemos e caracterizamos um software de neuronavegação compatível com vários rastreadores espaciais, o InVesalius Navigator. O algoritmo criado possibilitou o rastreamento de instrumentos por uma interface gráfica intuitiva. A precisão medida foi semelhante à de sistemas comerciais. Na segunda parte, imprimimos modelos 3D de pacientes com patologias neurológicas e avaliamos os erros de localização de marcos anatômicos durante a neuronavegação. Os erros de localização foram inferiores a 3 mm, considerados aceitáveis para aplicações clínicas. Por fim, na última parte, combinamos duas bobinas sobrepostas para controlar eletronicamente a orientação do CE, e investigamos como as respostas motoras evocadas dependem da orientação da corrente. A bobina desenvolvida possibilitou estimular o córtex motor com alta resolução angular. As respostas motoras apresentaram maior amplitude e menor latência para orientação do CE aproximadamente perpendicular ao sulco central. Em suma, esta tese fornece novos métodos para melhorar a precisão espacial de técnicas de intervenção com o cérebro.

Palavras-chave: Neuronavegação. Estimulação magnética transcraniana (EMT). Planejamento cirúrgico. Potencial evocado motor (PEM). Orientação da bobina. Impressão 3D.

# Abstract

**SOUZA, VHO. Development of instrumentation for neuronavigation and transcranial magnetic stimulation.** 2018. 74 f. Tese (Doutorado) – Faculdade de Filosofia, Ciências e Letras de Ribeirão Preto, Universidade de São Paulo, Ribeirão Preto, 2018.

Neuronavigation and transcranial magnetic stimulation (TMS) are valuable tools in clinical and research environment. Neuronavigation provides visual guidance of a given instrument during procedures of neurological interventions, relative to anatomic images. In turn, TMS allows the non-invasive study of cortical brain function and to treat several neurological disorders. Despite the well-accepted importance of both techniques, high-cost of neuronavigation systems and limited spatial accuracy of TMS in targeting brain structures, limit their applications. Therefore, the aim of this thesis was to i) develop an open-source, free neuronavigation software, ii) study a possible combination of neuronavigation and 3D printing for surgical planning, and iii) construct a multi-channel TMS coil with electronic control of electric field (E-field) orientation. In the first part, we developed and characterized a neuronavigation software compatible with multiple spatial tracking devices, the InVesalius Navigator. The created co-registration algorithm enabled tracking position and orientation of instruments with an intuitive graphical interface. Measured accuracy was similar to that of commercial systems. In the second part, we created 3D printed models from patients with neurological disorders and assessed the errors of localizing anatomical landmarks during neuronavigation. Localization errors were below 3 mm, considered acceptable for clinical applications. Finally, in the last part, we combined a set of two thin, overlapping coils to allow electronic control of the E-field orientation and investigated how the motor evoked responses depend on the stimulus orientation. The developed coil enabled the stimulation of the motor cortex with high angular resolution. Motor responses showed the highest amplitude and lowest latency with E-field approximately perpendicular to the central sulcus. In summary, this thesis provides new methods to improve spatial accuracy of techniques to brain interventions.

Keywords: Neuronavigation. Transcranial magnetic stimulation (TMS). Surgical planning. Motor evoked potentials (MEP). Coil orientation. 3D printing.

# List of Figures

- Figure 1.1:** Picture of an experimental set-up with a neuronavigation software connected to a tracking device that updates the position of a TMS coil relative to anatomical images. . 17
- Figure 1.2:** Schematic representation of TMS motor response. The TMS coil induces an E-field over the motor cortex, generating action potentials that propagate through the corticospinal tract to elicit MEPs. The amplitude and latency of MEPs can be measured using surface EMG. ....20
- Figure 2.1:** **A)** Picture of the acrylic phantom. The coordinate system indicates the axis SI, LR, and AP. **B)** Screenshot of InVesalius Navigator with phantom image slices in coronal, sagittal and axial view, and 3D visualization of points representing the crossing wires. Points were used for system characterization. Green markers represent the fiducials used for co-registration and red marker the real-time location of tracking device probe during navigation. ....26
- Figure 2.2:** InVesalius Navigator interface used to TMS coil positioning relative to a defined target. The distance to target is shown above the TMS coil in the central window, and the angular differences are represented by updating the arrows length in each direction, i.e., roll, yaw, and pitch, from top to bottom, on the right window of each screenshot. Each coil turns green if the coordinate difference is lower than the user-defined limits. **A)** Screenshots of navigation interface with all coil coordinates and **B)** only pitch rotation adjusted within limits predefined by the user. ....30
- Figure 2.3:** TRE distribution estimated for the cubic phantom used for characterization of **A)** InVesalius Navigator with MTC, **B)** InVesalius Navigator with Patriot, **C)** NBS 3.2 with Spectra and **D)** NBS 4.3 with Vicra. Red markers represent the location of fiducial points, and the four planes are located along the RL direction of the acrylic phantom. TRE for each point is represented by the color scale. .... 31
- Figure 2.4:** Accuracy error distribution measured for **A)** InVesalius Navigator with MTC and **B)** Patriot devices, and for **C)** NBS 3.2 with Spectra and **D)** NBS 4.3 with Vicra. Marker coordinates correspond to the crossing wires in the acrylic phantom assessed with the tracking device probe during neuronavigation. Colors indicate the average accuracy error across the three repetitions computed for each marker in the phantom. Red crosses represent the location of selected fiducial points. ....32
- Figure 2.5:** Measurements of accuracy error of InVesalius Navigator with MTC (Inv-MTC) and Patriot (Inv-Patriot), and NBS 3.2 with Spectra (NBS3.2-Spectra) and NBS 4.3 with Vicra (NBS4.3-Vicra). \*  $p < 0.05$  .....33
- Figure 2.6:** Difference between measurements of translation and rotation angles (yaw, pitch, and roll) to target during navigation with InVesalius Navigator connected to MTC and Patriot. The solid line represents the average, and dashed lines the 1.96 times the standard deviation (95% intervals) for each coordinate. ....34
- Figure 2.7:** Difference to the target in translation and rotation angles (yaw, pitch, and roll) in the experiment of accuracy for revisiting a target with InVesalius Navigator connected to MTC (Inv-MTC; white boxes) and Patriot (Inv-Patriot; gray boxes). \*  $p = 0.005$  .....35

- Figure 3.1:** **A)** 3D printed S1 model with the tracking probe of MTC. **B)** Neuronavigation markers are indicating top and bottom coordinates of each hole. **C)** Neuronavigation markers on three orthogonal planes and on **D)** sagittal plane view.....42
- Figure 3.2:** **A)** 3D printed model S2. **B)** Fiducial points (dark blue) and landmarks in the InVesalius volumetric view. Two markers representing one anatomical landmark are represented with the same color. AP-LH (green), AP-RH (pink), RL ears (dark blue), r-insula (cyan), r-cuneus (red) and r-prefrontal (orange). **C)** Markers were created during neuronavigation surrounding the perimeter of the head model and **D)** along the posterior gyrus of the central sulcus, for assessment of co-registration quality.....43
- Figure 3.3:** 3D printed scaled models of S2 and anatomical landmarks. **A)** Real size B100, half-sized (B50) and quarter-sized (B25) models. **B)** Frontal and back view of anatomical landmarks used for navigation and measurements: 1. RE, 2. N, 3. RFC, 4. RPC, 5. LPC, 6. ROC, 7. LOC, 8. LFC and 9. LE.....44
- Figure 3.4:** Boxplot of the distance measured on the six pairs of anatomical landmarks in each scaled model. LE-RE and RE-N showed higher distance values when measured in B25 compared to B50 and B100. \*\*\*  $p < 0.001$  .....47
- Figure 4.1:** Pipeline followed to obtain the current paths for a minimum-energy mTMS coil with electronic control of E-field orientation. Optimization algorithm uses the E-field distribution induced by a conventional, figure-of-eight coil in a spherical head surface. The target E-field has peak intensity of 100 V/m and was rotated between 0 and 180°. The minimum-energy current distributions were computed with constrains given in Table 4.1, and based on the target E-fields. Surface current densities, denoted by **J**, were decomposed in two components with orthogonal distributions to allow stimulation of E-field in any orientation parallel to the plane. Current values were normalized for visualization. Lastly, current distributions were discretized in 12 turns along the contour lines of its stream function. The resulting induced E-field has focality and distribution similar to that of the conventional figure-of-eight coil, but orientation can be adjusted by driving proportional currents in the top (solid orange lines) and bottom (solid black lines) paths. ....53
- Figure 4.2:** **A)** Virtual model of the designed coil formers. **B)** 3D-printed coil former with the copper wires wound in the top part (left) and bottom part (right)..... 54
- Figure 4.3:** **A)** E-field waveform generated by a monophasic current pulse with 60- $\mu$ s rise-time, with adjusted timing parameters. **B)** Measurement set-up of E-field calibration. The probe has two orthogonal 5-mm wire paths on the tip and rotates around a hemisphere with 70-mm radius. For each position, measurement was performed in both directions to provide the distribution and orientation of the E-field. ....56
- Figure 4.4:** Results obtained in the coil optimization procedure. Energy and E-field distribution were computed using the surface current distribution in the octagonal plane and were not affected by changing the number of loops. The gray square ( $\square$ ) highlights the coil model selected for production. ....58
- Figure 4.5:** Top and bottom graphs illustrate, respectively, the coil equivalent resistance and inductance measured for a range of sinusoidal waveforms with varying frequencies. Red solid lines represent the average value. ....59

**Figure 4.6:** **A)** Estimated normalized current required to induce an E-field in each orientation for the top (dashed line) and bottom (solid line) coils. **B)** E-field norm and orientation measured with the probe shown in Figure 4.3B. E-field was set to 25 V/m, and orientation varied from 0 to 180° in steps of 15°. The inserted box shows the differences between the set E-field ( $\Delta E$ ) and orientation ( $\Delta\theta$ ) values and measured values. ....60

**Figure 4.7:** **A)** Left and right plots show the normalized E-field profile in perpendicular (pink arrow) and parallel (red arrow) orientations, respectively. The central plot illustrates the induced E-field distribution in the spherical cortical surface with 70-mm radius for a TMS pulse at 0°. The shaded gray outer sphere represents the spherical scalp with an 85-mm radius. **B)** Vector plots of TMS induced E-fields at 45 and 90°. Color scale represents the normalized E-field norm.....61

**Figure 4.8:** Polar plots of average relative MEP amplitude and latency for each orientation of stimulus. The solid black line represents the harmonics fit and shaded area limited by the dashed line stands for the error of the fit. Each red or green dot represents the average relative MEP amplitude or latency across all subjects for a specific orientation, respectively. In the left, a schematic representation of the reference for defining the stimulus orientation is shown. 0° was the orientation in which the hotspot and motor threshold was measured, approximately perpendicular to the central sulcus.....62

# List of Tables

<b>Table 2.1:</b> Maximum FRE ( $FRE_{max}$ ) and maximum TRE ( $TRE_{max}$ ), average and 95 <sup>th</sup> percentile of accuracy error and average precision error for each navigation system. ....	31
<b>Table 2.2:</b> Repeatability as standard deviations and %StudyVar estimated in a Gage R & R study. ....	34
<b>Table 3.1:</b> Measurements of distance between surface and bottom of each hole in the brain model. ....	45
<b>Table 3.2:</b> Euclidean distance of anatomical landmarks estimated by one rater in InVesalius interface, with a caliper and during navigation (Navigation 1), and by a second rater only during navigation (Navigation 2). ....	46
<b>Table 4.1:</b> Constraints used for the coil optimization, adapted from Koponen et al. (2015, 2017). $E_{\parallel,0}$ and $E_{\perp,0}$ are the parallel and perpendicular components of induced E-field at the focal point. ....	51
<b>Table 4.2:</b> Values tested for each parameter during coil optimization. ....	52

# List of Abbreviations

<b>%StudyVar</b>	Percentage of study variation
<b>3D</b>	Three-dimensional
<b>AI</b>	Anisotropy index
<b>ANOVA</b>	Analysis of variance
<b>AP</b>	Anterior-posterior
<b>CT</b>	Computed tomography
<b>CV</b>	Coefficient of variation
<b>E-field</b>	Electric field
<b>EMG</b>	Electromyography
<b>FRE</b>	Fiducial registration error
<b>FRE<sub>max</sub></b>	Maximum fiducial registration error
<b>FWHM</b>	Full-width at half-maximum
<b>LE</b>	Left ear
<b>LFC</b>	Left frontal cortex
<b>LH</b>	Left hemisphere
<b>LOC</b>	Left occipital cortex
<b>LPC</b>	Left parietal cortex
<b>MEP</b>	Motor evoked potential
<b>MRI</b>	Magnetic resonance imaging
<b>MTC</b>	MicronTracker
<b>mTMS</b>	Multi-locus transcranial magnetic stimulation
<b>N</b>	Nasion
<b>PLA</b>	Polylactic acid
<b>r-cuneus</b>	Right cuneus
<b>RE</b>	Right ear
<b>RFC</b>	Right frontal cortex
<b>RH</b>	Right hemisphere
<b>r-insula</b>	Right insula

<b>RL</b>	Right-left
<b>ROC</b>	Right occipital cortex
<b>RPC</b>	Right parietal cortex
<b>r-prefrontal</b>	Right prefrontal cortex
<b>SDK</b>	Software development kit
<b>SI</b>	Superior-inferior
<b>STL</b>	Stereolithography
<b>TMS</b>	Transcranial magnetic stimulation
<b>TRE</b>	Target registration error
<b>TRE<sub>max</sub></b>	Maximum target registration error

# Contents

<b>1. INTRODUCTION .....</b>	<b>17</b>
1.1 Neuronavigation .....	17
1.1.1 Patient-specific models for neurosurgery .....	18
1.2 Transcranial magnetic stimulation .....	19
1.3 Objectives and thesis organization .....	22
<b>2. DEVELOPMENT AND CHARACTERIZATION OF THE NEURONAVIGATION SOFTWARE .....</b>	<b>23</b>
2.1 Introduction .....	23
2.2 Material and methods .....	23
2.2.1 Software development .....	23
2.2.2 Co-registration method .....	24
2.2.3 Validation of co-registration method.....	25
2.2.3.1 Phantom design .....	25
2.2.3.2 Experimental procedure.....	26
2.2.3.3 Data analysis.....	27
2.3 Validation of object position and orientation control.....	28
2.3.1 Accuracy for revisiting a target .....	29
2.4 Results .....	30
2.4.1 Software validation.....	30
2.4.2 Control of coil position and orientation.....	33
2.4.3 Accuracy for revisiting a target .....	34
2.5 Discussion.....	35
2.5.1 Navigation pipeline and general features .....	35
2.5.2 Software validation.....	36
2.5.3 InVesalius Navigator for coil positioning .....	38
2.6 Conclusion.....	40
<b>3. NEURONAVIGATION AND PATIENT-SPECIFIC MODELS .....</b>	<b>41</b>
3.1 Introduction .....	41
3.2 Material and methods .....	41
3.2.1 Patient-specific models.....	41
3.2.2 Errors of neuronavigation in patient-specific models.....	42
3.2.3 Scaling effects on patient-specific models .....	44
3.2.3.1 Statistical analysis .....	45

3.3	Results .....	45
3.3.1	Errors of neuronavigation in patient-specific models.....	45
3.3.2	Scaling effects on patient-specific models .....	46
3.4	Discussion.....	47
3.5	Conclusion.....	49
<b>4.</b>	<b>TMS COIL WITH ELECTRONIC CONTROL OF E-FIELD ORIENTATION ...</b>	<b>50</b>
4.1	Introduction .....	50
4.2	Material and methods .....	50
4.2.1	Optimization parameters.....	50
4.2.2	Coil manufacturing and calibration .....	54
4.2.3	Assessment of motor cortex orientation-dependency.....	56
4.2.4	Data analysis.....	57
4.3	Results .....	58
4.3.1	Coil optimization and validation .....	58
4.3.2	Motor cortex orientation-dependency .....	61
4.4	Discussion.....	62
4.4.1	Developed mTMS coil .....	62
4.4.2	Motor cortex orientation-dependency .....	64
4.5	Conclusion.....	66
<b>5.</b>	<b>FINAL REMARKS .....</b>	<b>67</b>
<b>6.</b>	<b>REFERENCES .....</b>	<b>68</b>
	<b>APPENDIX A.....</b>	<b>74</b>

# 1. Introduction

## 1.1 Neuronavigation

Neuronavigation systems have been shown to be a valuable tool in clinical and research applications. A combination of spatial tracking devices and tomographic neuroimages, such as computed tomography (CT) and magnetic resonance imaging (MRI), allows accurate and real-time localization of surgical and interventional instruments with respect to neuronal anatomy. By incorporating neuronavigation into functional brain imaging techniques, it is possible to register and locate the recording sensors, e.g., electroencephalography (Chiarelli et al., 2015), magnetoencephalography (Little et al., 2014) and optical diffusion spectroscopy (Tsuzuki and Dan, 2014), and provide accurate and stable positioning of a transcranial magnetic stimulation (TMS) coil throughout the session (Ruohonen and Karhu, 2010), Figure 1.1.

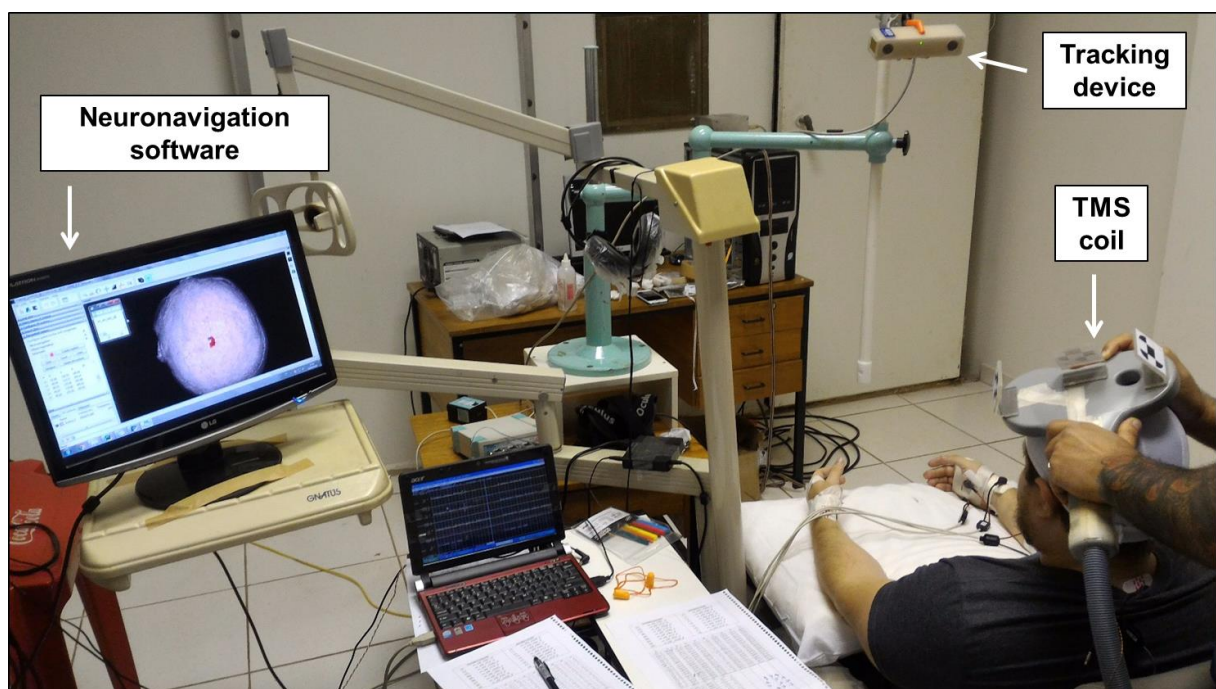


**Figure 1.1:** Picture of an experimental set-up with a neuronavigation software connected to a tracking device that updates the position of a TMS coil relative to anatomical images.

Despite the well-accepted benefits of navigation systems, the high-cost, which typically range from \$ 50,000 to \$ 150,000, sophisticated technology and availability of MRI facilities limits its insertion in research and clinical environment. Therefore, low-cost alternatives are of utmost importance. Recently, Ambronisi et al. (2018) developed the StimTrack software for

online TMS coil placement without the need of MRI. Moreover, several open-source projects aimed at the development of image-guided navigation for surgical applications, such as CustuX, SlicerIGT (Fedorov et al., 2012), MITK-ITC (Nolden et al., 2013) and NiftyIGI (Clarkson et al., 2015). However, none of these frameworks provide specific tools for image-guided coil placement in TMS.

In the context of free software for neuroscientific research, Python language has evolved considerably in the last decades. Python has been used by many important packages and software in neuroscience, e.g., MNE (Gramfort, 2013), PsychoPy (Peirce, 2007), MagPy (McNair, 2017). The ability to interface with different languages, easy syntax, high-level coding and a vast number of libraries turns Python into a suitable language for community maintained and open-source projects. In this sense, InVesalius has been developed and written in Python, as multiplatform and free software since 2001 by the Information Technology Center Renato Archer in Campinas, Brazil (Amorim et al., 2015). InVesalius has tools for medical image visualization, user-friendly simplistic interface, is translated to 16 languages and is compatible with Microsoft Windows, Linux, and MacOS platforms. In addition, InVesalius has an active worldwide community of contributors with users in 144 countries. Altogether, these features make InVesalius a suitable platform for the development of a free neuronavigation software.

### **1.1.1 Patient-specific models for neurosurgery**

Multimodal visualization tools offer critical evidence of eloquent areas and surgical trajectories better suited to improve the prognosis of patients undergoing neurosurgery. In general, planning is performed by analysis of MRI or CT imaging software, and discussions among all responsible professionals. In this context, surgical planning combined with neuronavigation in patient-specific brain models is a tool with the potential to aid surgeons during the preparation phase and determination of strategies to be adopted (Rondinoni et al., 2014; Vannier et al., 1984). Grouping these two techniques allows the specialists to evaluate surgical maneuvers with specific information of anatomical references of each patient. However, the combination of patient-specific models and neuronavigation for surgical planning still lacks validations to promote its use in a clinical environment (Wu et al., 2008).

Patient-specific models represent the anatomy of each individual realistically and result from a complicated process. The process begins in the acquisition of the tomographic images, going through the computational processing of data and ends with the creation and three-

dimensional (3D) printing of the virtual models (Cooper and Taqueti, 2008; Filho et al., 2011). Several high-cost devices and the participation of specific human resources are required. Furthermore, the materials and equipment used during production might have a critical impact on the quality of the final model (Choi et al., 2002). The use of 3D printing in medicine is a relatively recent field of research, with great potential to provide more individualized treatments (Grillo et al., 2018). In this context, many studies are required to investigate the applicability of the technology in clinical routine.

## **1.2 Transcranial magnetic stimulation**

TMS was first introduced by Barker et al. (1985) and currently is an important tool for non-invasive brain stimulation (Hallett, 2000; Wassermann and Zimmermann, 2012). Magnetic pulses generated by a coil positioned externally over the primary motor cortex induce electric fields (E-fields) in the cortical tissue, depolarizing neurons. The resulting action potentials travel through the corticospinal tract reaching the spinal motor neurons and, finally, the target muscle, illustrated in Figure 1.2. The myoelectric activity produced in response to TMS is called motor evoked potential (MEP) and is commonly recorded by surface electromyography (EMG) (Garcia et al., 2017; Wassermann et al., 1992). The amplitude and latency are the descriptors of MEPs of primary clinical interest, used in studies of cerebral physiology (Rossini et al., 2015) and to evaluate damage to the motor cortex and corticospinal tract (Peres et al., 2017; Rossini et al., 2015; Ziemann, 2000).

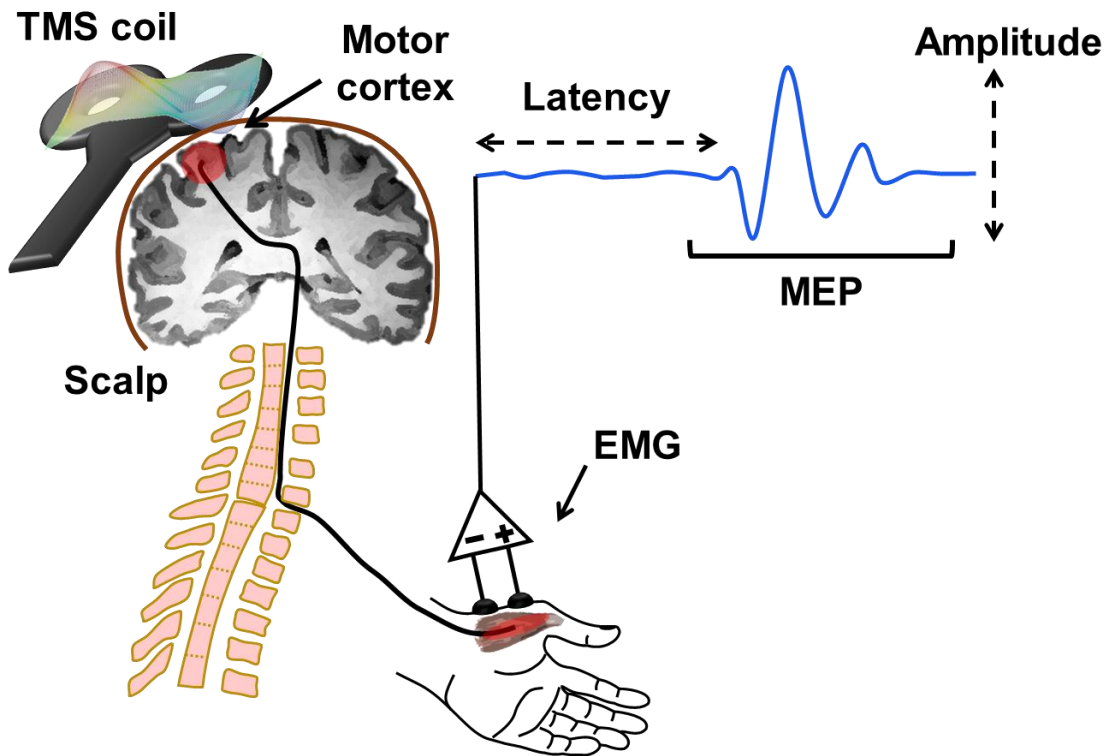


**Figure 1.2:** Schematic representation of TMS motor response. The TMS coil induces an E-field over the motor cortex, generating action potentials that propagate through the corticospinal tract to elicit MEPs. The amplitude and latency of MEPs can be measured using surface EMG.

The underlying physical principle of TMS follows the electromagnetic laws of induction (Neggers et al., 2015; Wassermann et al., 2012). A high current driven in a coil for a brief interval generates an intense, time-varying magnetic field. The biological tissues have magnetic permeability similar to that of the vacuum. Therefore, the magnetic field penetrates the scalp and skull and induces an E-field in the conducting cortical surface, given by the Faraday's law of induction in Equation 1.1. In turn, the E-field influences the charged particles in the conducting medium of the cerebral cortex, e.g., neuron's membranes, creating a current flow, as in Equation 1.2.

$$\nabla \times \mathbf{E} = -\frac{\partial \mathbf{B}}{\partial t} \quad (1.1)$$

$$\mathbf{J} = \sigma \mathbf{E} \quad (1.2)$$

where  $\mathbf{E}$  is the E-field,  $\mathbf{B}$  the magnetic field,  $\mathbf{J}$  the current density and  $\sigma$  the tissue conductivity. The simplest circuit necessary to generate a TMS pulse is composed by a voltage source, a capacitor, a resistor, a solid-state switch and an inductor, i.e., the TMS coil. When the

switch is closed, the capacitor rapidly discharges a current through the wires of the coil and generates the magnetic field. Nowadays, much more complex circuits have been developed to allow full control of current's waveform (Koponen et al., 2017; Peterchev et al., 2014).

Combining two adjacent circular coils with currents flowing in opposite directions induces a relatively focal and oriented E-field distribution in the cortex. This specific design is the most used for TMS and is named figure-of-eight, or butterfly coil (Ueno et al., 1988), see Figure 1.2. Furthermore, combining several coils in different designs lead to distinct E-field distributions (Deng et al., 2008). By adequately composing many coils with independent, driven currents, it is possible to shape the induced E-field distribution electronically. The electronic control of E-field distribution was initially studied in the late 1990's (Ruohonen et al., 1999; Ruohonen and Ilmoniemi, 1998), and named as multi-channel TMS. However, the proposed arrays of coils have critical limitations regarding the power required to evoke measurable physiological responses in the brain. Recently, Koponen et al. (2017, 2015) developed new methods for the manufacturing of minimum-energy TMS coils capable of stimulating the brain with considerably less power requirements. Furthermore, by superimposing such minimum-energy coils might be possible to automatically control the position and orientation of the E-field distribution (Koponen, 2013).

It is important to mention that physiological responses to TMS depend on many different stimulation parameters. Specifically, the effect of coil orientation on MEP amplitude and latency has been extensively studied (D'Ostilio et al., 2016; Hannah and Rothwell, 2017; Kallioniemi et al., 2015a; Souza et al., 2017). It is a consensus that E-field approximately perpendicular to the primary motor cortex, and the current flowing in the coil in posterior-anterior direction is the orientation that elicits MEPs in intrinsic hand muscles with the highest amplitude and lower latencies (Di Lazzaro et al., 2008; Rossini et al., 2015). In this orientation, the current induced across the sulci and gyri is mainly parallel to the pyramidal neurons. Therefore, a higher amplitude of the E-field along the axons and synapses connections might be favorable to fire action potentials in a higher population of motor neurons. Also, E-field oriented in lateral-medial direction might result in lower amplitudes and preferably direct activate the neuronal axons, leading to lower latencies (Di Lazzaro et al., 2008; Werhahn et al., 1994). Moreover, the orientation-dependency of MEP in the primary motor cortex is highly variable across subjects and strongly affected by the presence of neurological disorders (Kallioniemi et al., 2015a).

Current commercially available devices require manual adjustment of the coil over the scalp to target a desired single, localized area in a specific E-field orientation. Manual

placement contributes to an increase in MEP variability and makes challenging the control of coil location and orientation. Neuronavigation systems have been used to improve positioning accuracy and control of the TMS coil, using spatial tracking and an MRI-guided interface (Ruohonen and Karhu, 2010). Even with the aid of neuronavigation, the influence of manually holding the coil to change orientation and position might still contribute to a considerable portion of total accuracy error. In this context, a device that automatically adjusts the coil orientation relative to each individual anatomy would probably improve the reliability of MEP recordings and the efficacy of TMS.

### **1.3 Objectives and thesis organization**

This thesis aims to:

- i. Develop and validate an open-source, free neuronavigation software with tools for accurate localization of an instrument relative to anatomical images;
- ii. Study the possible combination of 3D-printed patient-specific models and neuronavigation for surgical planning;
- iii. Construct a multichannel TMS coil to allow electronic control of E-field orientation and study the orientation-dependency of MEPs with high angular resolution.

In Chapter 2 we describe the developed co-registration algorithm for neuronavigation and discuss the results obtained in a series of validation and characterization experiments. Next, in Chapter 3 we assess the errors in the localization of anatomical structures during neuronavigation in patient-specific models and discuss the possible combination of the two techniques for surgical planning. Then, we report in Chapter 4 the methods applied to manufacture a multichannel TMS coil with electronic control of E-field orientation, and the orientation-dependency of MEPs studied with high angular resolution. Lastly, we summarize our conclusions in Chapter 5.

## 2. Development and characterization of the neuronavigation software

---

### 2.1 Introduction

To overcome the limitations of current navigation software, we developed an extension of InVesalius, the InVesalius Navigator, to provide communication with multiple tracking devices, tools for processing structural MRI and online TMS coil tracking, all combined in a user-friendly interface. This chapter aims to describe the navigation pipeline developed for InVesalius Navigator and estimate the errors associated with the navigation procedure in a phantom and a simulated TMS study. Moreover, we compared the errors with a commercially available device for navigated TMS.

### 2.2 Material and methods

#### 2.2.1 Software development

InVesalius Navigator was written in Python 2.7 combined with several freely available libraries, such as wxPython 3.0 for the graphical user interface, Visualization Toolkit 6.3 for visualization tools, Nibabel 2.0 for neuroimage support and Numpy 1.11 for numerical data and array manipulation. A complete list of dependencies and download links are available in the InVesalius project website [<https://www.cti.gov.br/invesalius>].

Wrapping libraries were developed to enable access to the software development kit (SDK) of commercial spatial tracking devices. Communication to the following models was developed: MicronTracker (MTC) Sx60 (ClaroNav Inc., Toronto, Canada), Patriot, Fastrak and Isotrak II (Polhemus, Colchester, VT, USA). A combination of CMake (Kitware, Inc., Clifton Park, NY, USA), Swigwin (University of Utah, Salt Lake City, UT, USA) and Visual Community 2015 (Microsoft Corporation, Redmond, WA, USA) was used to generate and compile C++ libraries and the source code of each SDK, resulting in a portable Python package. Generated libraries are available with other dependencies packages in the InVesalius repository on GitHub [<https://github.com/invesalius/invesalius3>]. Since no commercial source code is accessible within the wrapping libraries, all companies approved their distribution.

### 2.2.2 Co-registration method

The co-registration algorithm is a set of matrix multiplications that transforms coordinates in the tracking device reference frame, i.e., physical space, to the user interface scene in the software, i.e., virtual space. Three tracking sensors are used during the procedure, a probe to record the fiducial points, a reference sensor attached to a rigid part of the head, e.g., forehead, and a third sensor attached to the tracked object, e.g., a TMS coil. All the computations are performed using affine transformations with homogeneous coordinates to represent a translation  $T$ , a rotation  $R$  or translation followed by a rotation given by  $M$ , no shearing and scaling is used.

Translation and rotation of the object are split into two steps. The translation first requires applying an offset from the fixed position of the sensor in the object to the point of interest the user needs to track, e.g., center of the coil. Thus, a reference frame of the coil is created by collecting three fiducials distributed around the point of interest in the tracking device reference frame and then computing a change of basis matrix  ${}_{\text{base}}^{\text{obj}}M_{\text{trk}}$ , using a custom-made method described in Appendix A. During this step the object must be fixed with the third sensor attached. The initial position and orientation of the attached sensor given in the tracker reference frame is  ${}^{\text{obj}}M_{0_{\text{trk}}}$ , a composition of a rotation  ${}^{\text{obj}}R_{0_{\text{trk}}}$  and a translation  ${}^{\text{obj}}T_{0_{\text{trk}}}$ . The offset to the point of interest is then applied in every iteration during the navigation with the following equation:

$${}^{\text{obj}}M_{\text{trk}} = \text{probe}R_{\text{trk}}(\text{probe}M_{0_{\text{trk}}})^{-1}(\text{probe}R_{0_{\text{trk}}})^{-1}\text{probe}R_{\text{trk}}{}_{\text{base}}^{\text{obj}}M_{\text{trk}}\text{probe}M_{0_{\text{trk}}}\text{probe}T_{\text{trk}} \quad (2.1)$$

where  $\text{probe}R_{\text{trk}}$  and  $\text{probe}T_{\text{trk}}$  are the instantaneous probe rotation and translation in tracking reference frame. Next, the coordinate of the object is transformed to the reference sensor attached to the head, to correct for possible movements of the subject.

$${}^{\text{obj}}M_{\text{ref}} = {}^{\text{ref}}M_{\text{trk}}^{-1}{}^{\text{obj}}M_{\text{trk}} \quad (2.2)$$

where  ${}^{\text{obj}}M_{\text{ref}}$  is the object transformation matrix given in the head reference sensor frame. Then, we apply the change from real to virtual space using  ${}^{\text{img}}M_{\text{ref}}$  in two separate steps for rotation and translation.  ${}^{\text{img}}M_{\text{ref}}$  is computed using the quaternion-based algorithm by Horn

et al. (1987) and three fiducials collected in the nasion, left and right tragus with coordinates given in both virtual space and tracker reference space. Thus, the translation and rotation are given by:

$${}^{\text{obj}}T_{\text{img}} = {}^{\text{img}}M_{\text{ref}} {}^{\text{obj}}M_{\text{ref}} \quad (2.3)$$

$${}^{\text{obj}}R_{\text{img}} = {}^{\text{obj}}R_{\text{img}} ({}^{\text{base}}M_{\text{trk}})^{-1} ({}^{\text{obj}}M_{0_{\text{ref}}})^{-1} {}^{\text{obj}}M_{\text{ref}} {}^{\text{base}}M_{\text{trk}} \quad (2.4)$$

where  ${}^{\text{obj}}R_{\text{img}}$  is the rotation component of a change of basis matrix computed with the method shown in Appendix A and the object fiducials given in the virtual space. Finally, the affine matrix is composed using the translation represented in homogeneous coordinates by  ${}^{\text{obj}}T_{\text{img}}$  and the (3 x 3) rotation matrix component in  ${}^{\text{obj}}R_{\text{img}}$ . The result is the transformation matrix  ${}^{\text{obj}}M_{\text{img}}$  that is directly applied to the virtual object in the visualization scene.

## 2.2.3 Validation of co-registration method

### 2.2.3.1 Phantom design

A cubic acrylic phantom with  $211.00 \pm 0.05$  mm length was used for characterization of the navigation system (Figure 2.1A), designed with dimensions comparable to the average human head. 3D axes were named as anterior-posterior (AP), right-left (RL) and superior-inferior (SI) for correspondence with conventional medical imaging orientation system. Nylon wires with  $0.25 \pm 0.05$  mm diameter were interlaced inside the acrylic cube composing an inner cube with an edge length of  $100.00 \pm 0.05$  mm and 1331 intersecting points. Every crossing point in the inner cube was distant from its first neighbors by  $10.00 \pm 0.05$  mm in all axes.

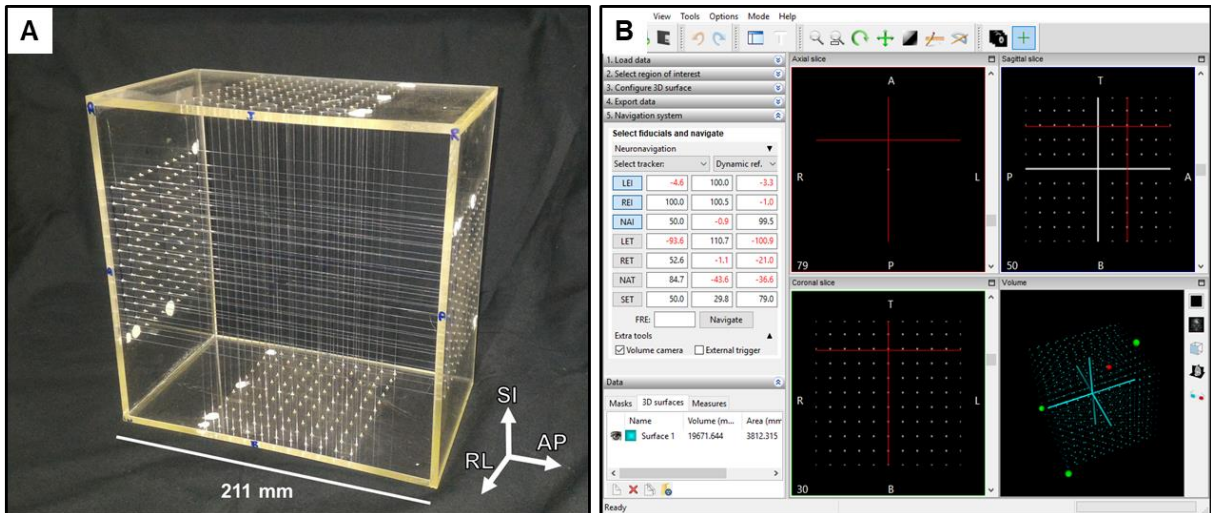


**Figure 2.1:** **A)** Picture of the acrylic phantom. The coordinate system indicates the axis SI, LR, and AP. **B)** Screenshot of InVesalius Navigator with phantom image slices in coronal, sagittal and axial view, and 3D visualization of points representing the crossing wires. Points were used for system characterization. Green markers represent the fiducials used for co-registration and red marker the real-time location of tracking device probe during navigation.

Virtual tomographic images of the cubic phantom were produced using a MATLAB 2013a (MathWorks Inc., Natick, MT, USA). A script was written to overwrite the pixel values in a real subject's MRI. MRI was acquired with a conventional 3D T1-weighted gradient echo sequence, repetition time of 6.7 ms, echo time of 3.1 ms and (256 x 265 x 180) acquisition matrix with pixel size of (1 x 1 x 1) mm<sup>3</sup>. Each crossing point in the acrylic phantom was represented by a voxel value of 255, resulting in a framed virtual cube in the MRI with an edge length of 100 mm, and identical to the measurement volume of the acrylic phantom. All personal information of the subject was removed from the images.

### 2.2.3.2 Experimental procedure

The experiment was performed in distinct sessions using InVesalius Navigator connected to MTC and Patriot. For comparison with commercial devices, an additional experiment was performed with NBS 3.2, and NBS 4.3 (Nexstim Plc, Helsinki, Finland) connected to the optical tracking systems Polaris Spectra and Vicra (Northern Digital Inc., Waterloo, ON, Canada), respectively.

Phantom images were imported to the correspondent navigation software and split in axial, sagittal and coronal views. Next, a volumetric reconstruction of all measurement points was created to obtain 1.0 mm diameter spheres in the volumetric rendering space, shown in InVesalius Navigator screen in Figure 2.1B. For co-registration, fiducials were selected to

## InVesalius Navigator software

resemble the locations of nasion, left and right ears commonly used in human applications. Selected fiducials were right and left extremities of the intersection line between the posterior and inferior planes, and the midpoint of the intersection line between the anterior and superior planes. Recording of coordinates was performed using the digitization function available in InVesalius Navigator and NBS.

Measurements were performed placing the tip of the tracking probe and digitizing the coordinates of each crossing point in four planes along the RL axis. Within each plane, i.e., in AP and SI axis, points were located every  $10.00 \pm 0.05$  mm in all axis. Plane one was close to the cube's left face. Distances between planes number two, three and four to plane one; were  $10.00 \pm 0.05$  mm,  $50.00 \pm 0.05$  mm and  $100.00 \pm 0.05$  mm, respectively. Inner cube had an edge length of  $100.00 \pm 0.05$  mm, composing the measurement volume. Measurement sequence started from the point in the upper anterior corner of the phantom. The experiment was performed within the operational range provided by the manufacturers of all tracking devices, 152 cm for Patriot, 115 cm for MTC, 134 cm for Vicra and 240 cm for Spectra. The entire procedure was repeated three times by the same operator.

### 2.2.3.3 Data analysis

Analysis consisted in computing the error related solely to the developed co-registration algorithm with the fiducial registration error (FRE). Then, the error of targeting a point in space was estimated for the given fiducial configuration using the target registration error (TRE). Overall system accuracy and precision errors during the navigation procedure were computed. FRE was computed as the root mean square distance from the fiducial coordinates to its counterpart after the co-registration (Fitzpatrick et al., 1998), given by:

$$FRE^2 \equiv \frac{1}{n} \sum_{i=1}^n \left| \left( Q_E + (M^{-1} \cdot N)(P_{Hi} - Q_H) \right) - P_i \right|^2 \quad (2.5)$$

where  $P_i$  is the image fiducial  $i$ ,  $P_{Hi}$  the correspondent fiducial in the tracker reference frame and  $n$  is the total number of fiducials. In turn, the TRE represents the distance between a target point other than fiducials and its counterpart after co-registration. TRE was estimated as proposed by Fitzpatrick et al. (1998):

$$\langle \text{TRE}^2(\mathbf{r}) \rangle \approx \frac{\langle \text{FRE}^2 \rangle}{(n-2)} \left( 1 + \frac{1}{3} \sum_{k=1}^3 \frac{d_k^2}{f_k^2} \right) \quad (2.6)$$

where the given fiducials configuration results in a principal axis  $k$ ,  $f_k$  is the root mean square distance between the fiducials to the principal axis and  $d_k$  is the distance between the target to the principal axis. TRE was estimated using the maximum FRE obtained among all characterization runs for a given device.

The accuracy error was defined as the Euclidian distance between coordinates measured in image space during navigation and the actual coordinate in the simulated phantom image. Average accuracy error was estimated across all 484 points for each navigation system. Precision was estimated as the standard deviation of the average accuracy error (Kuehn et al., 2008).

One-way analysis of variance (ANOVA) was applied to investigate how accuracy error differed between navigation systems; residual plots did not reveal any apparent deviations from normality. Tukey HSD was used for post hoc multiple comparisons. Statistical analysis was performed in R 3.4 (R Core Team, Vienna, Austria) and the level of significance was set at 5%.

## 2.3 Validation of object position and orientation control

A dummy head and a TMS figure-of-eight coil (Neurosoft, Ivanovo, Russia) were used to compute the repeatability of estimating the rotation angles and translation vector during navigation, in an experiment like described in Ambrosini et al. (2018). The dummy head was filled with a solution composed of 3.6 g of NaCl and 1.95 g of  $\text{CuSO}_4 \cdot 5\text{H}_2\text{O}$  per liter of  $\text{H}_2\text{O}$  (Och et al., 1992; Peres et al., 2009). MRI of the head was acquired in a scanner Achieva 3T (Philips Healthcare, Best, The Netherlands) with a gradient echo sequence, acquisition matrix of (256 x 256 x 156) mm, FOV of 256 mm and a voxel size of (1 x 1 x 1) mm. MRI was imported to InVesalius Navigator for co-registration using nasion, right and left tragus fiducials. The dummy head was attached to a table, and the coil held with a mechanical arm and centered over the approximate area of the hand knob in the primary motor cortex. Measurements of the transformation matrix were performed in three experimental conditions for two different targets, the left, and right hand knobs. For each target three conditions were used: a head sensor in position one and coil registration one, the head sensor in position two and coil registration one and head sensor in position two and coil registration two. Co-registration was repeated ten

times, and the translation vector and rotation angles were extracted from the transformation matrix in each trial. An additional run was executed with the head sensor in position two and coil registration one to evaluate the static fluctuations of coordinates during navigation. In this case, coordinates were sampled every 2 seconds for 180 seconds, with coil and head static during navigation. The whole experiment was performed separately for MTC and Patriot tracking devices.

Repeatability was estimated for the translation vector, i.e., Euclidian distance, and angle difference to the saved target coordinates using the Gage R & R measurement system assessment in SixSigma package of software R 3.4.0 (R Core Team).

### **2.3.1 Accuracy for revisiting a target**

InVesalius Navigator accuracy error associated with repositioning the stimulation coil multiple times relative to a defined target was estimated in a simulated TMS experiment. Three adults (two men and one woman, 24, 26 and 29 years old), with non-reported neurological or motor diseases, participated in this study. All subjects were submitted to a volumetric gradient echo T1-weighted MRI in a scanner Achieva 3T (Philips Healthcare) with (240 x 240 x 240) acquisition matrix and a voxel size of (1 x 1 x 1) mm. The study was approved by the local ethics committee of the University of São Paulo (CAAE: 54674416.9.0000.5407) in accordance with the Declaration of Helsinki. The experiment was performed after each participant gave written informed consent.

Participants sat comfortably in a reclining chair and were asked to stay fully relaxed, following the same procedures as in a conventional TMS experiment (Julkunen, 2014). MRI was imported to InVesalius Navigator, a volumetric rendering was constructed, and co-registration performed using the fiducials nasion, left and right tragus. The hand knob in the left primary motor cortex is commonly used in TMS experiments and was marked as the target. A TMS figure-of-eight coil was positioned approximately tangential to the scalp, directly above the target and saved in InVesalius Navigator. Coil was initially placed on a table by the left side of the subject. The coil was moved from the initial position to the target following the InVesalius Navigator guiding interface, shown in Figure 2.2. When the user was able to hold the coil steady within the range of 3 mm for distance and 3° for each rotation angle, a marker was created, and the coil returned to the initial position. This procedure was repeated ten times for three head co-registrations and with InVesalius Navigator connected separately to MTC and Patriot.

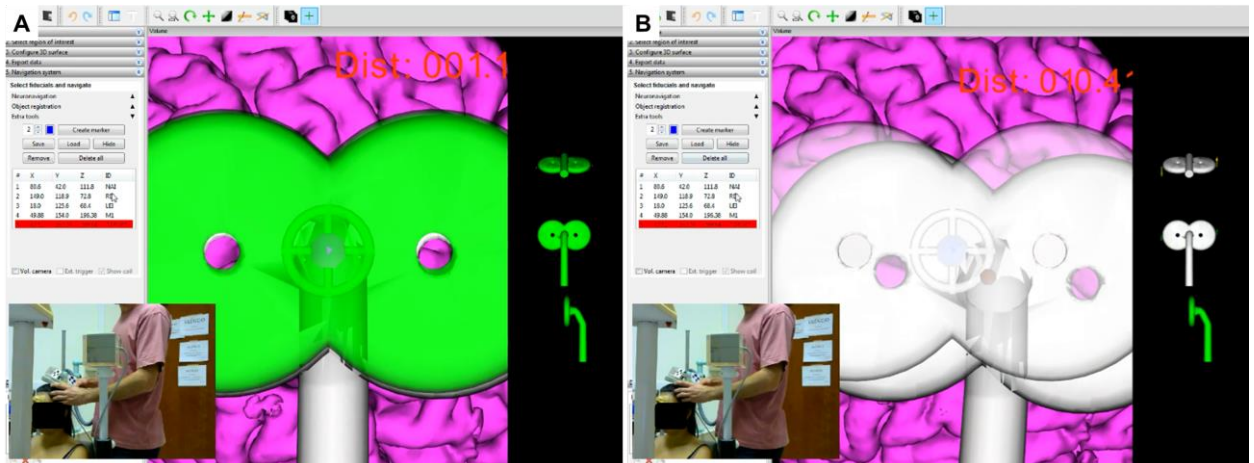


**Figure 2.2:** InVesalius Navigator interface used to TMS coil positioning relative to a defined target. The distance to target is shown above the TMS coil in the central window, and the angular differences are represented by updating the arrows length in each direction, i.e., roll, yaw, and pitch, from top to bottom, on the right window of each screenshot. Each coil turns green if the coordinate difference is lower than the user-defined limits. **A)** Screenshots of navigation interface with all coil coordinates and **B)** only pitch rotation adjusted within limits predefined by the user.

Accuracy error associated with revisiting a target was computed as the average Euclidian distance and angle deviations in each axis between every marker and the correspondent target. Two-way ANOVA was used to investigate if differences in coordinates vary for each tracking device (MTC and Patriot) and coordinate (translation, yaw, pitch, and roll). Post hoc multiple comparisons were performed using Tukey HSD test and level of significance was set at 5%.

## 2.4 Results

### 2.4.1 Software validation

The FRE, TRE, mean accuracy and precision errors for InVesalius Navigator connected to MTC and Patriot, and NBS 3.4, NBS 4.2 connected to Spectra and Vicra devices are depicted in Table 2.1. TRE and accuracy error spatial distributions of measurements in the acrylic cubic phantom for all tested systems are illustrated in Figure 2.3 and Figure 2.4, respectively.

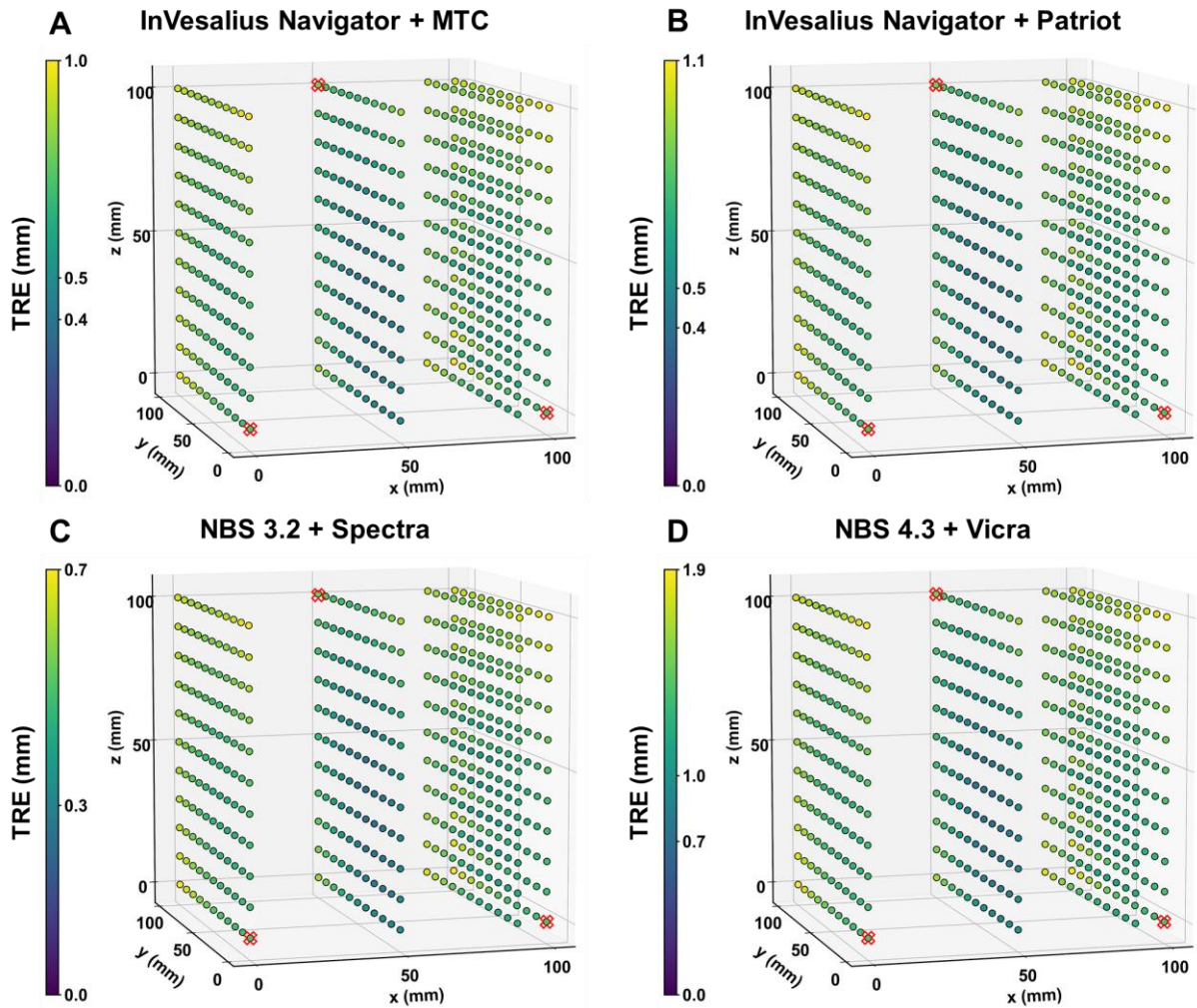


**Figure 2.3:** TRE distribution estimated for the cubic phantom used for characterization of **A)** InVesalius Navigator with MTC, **B)** InVesalius Navigator with Patriot, **C)** NBS 3.2 with Spectra and **D)** NBS 4.3 with Vicra. Red markers represent the location of fiducial points, and the four planes are located along the RL direction of the acrylic phantom. TRE for each point is represented by the color scale.

**Table 2.1:** Maximum FRE ( $FRE_{max}$ ) and maximum TRE ( $TRE_{max}$ ), average and 95<sup>th</sup> percentile of accuracy error and average precision error for each navigation system.

Navigation system	$FRE_{max}$ (mm)	$TRE_{max}$ (mm)	Accuracy (mm)	95 <sup>th</sup> percentile (mm)	Precision (mm)
MTC	0.38	1.02	1.46	2.41	0.52
Patriot	0.40	1.08	1.52	2.55	0.58
Spectra	0.25	0.67	1.12	2.11	0.46
Vicra	0.72	1.94	1.17	2.29	0.56

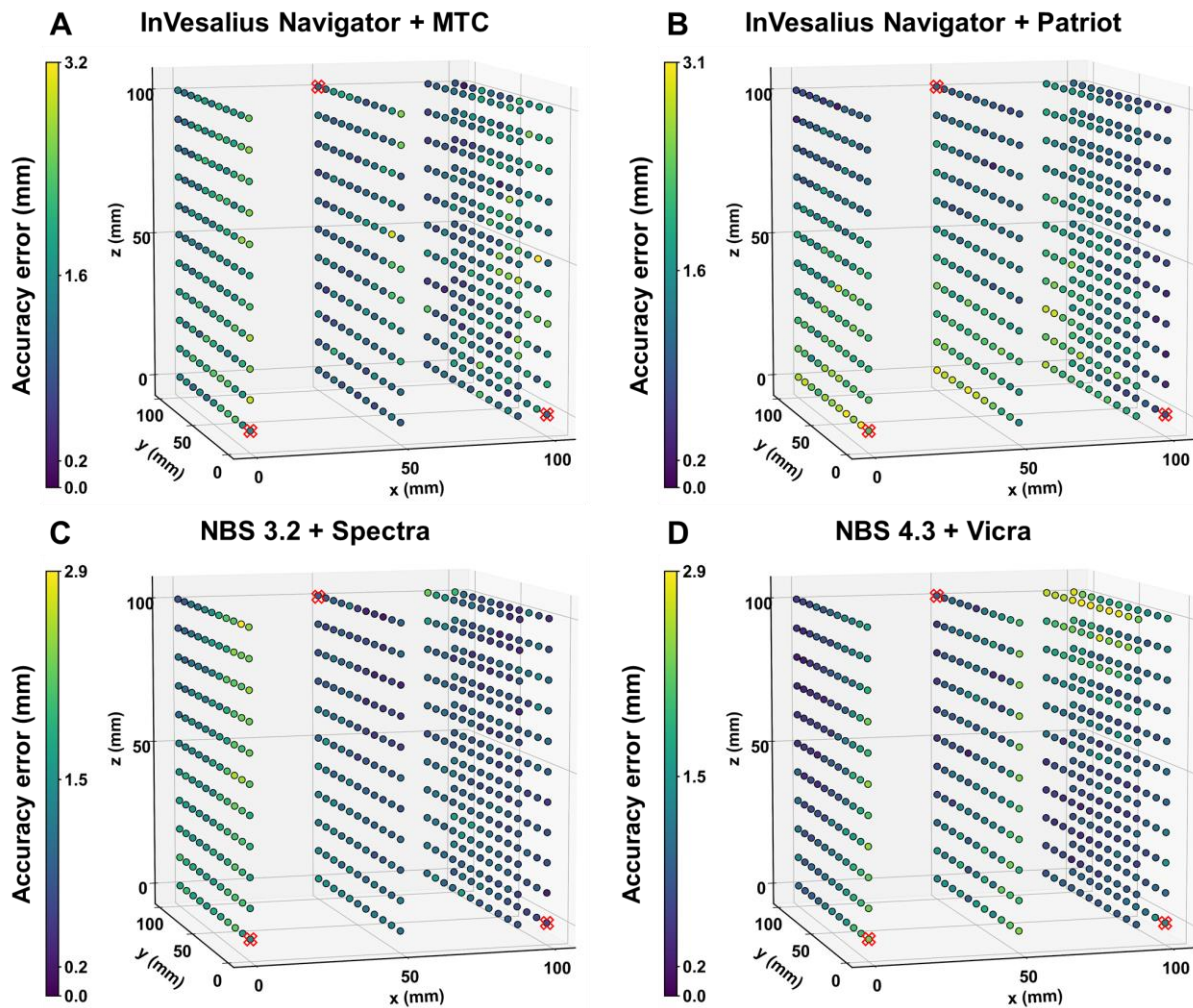


**Figure 2.4:** Accuracy error distribution measured for **A)** InVesalius Navigator with MTC and **B)** Patriot devices, and for **C)** NBS 3.2 with Spectra and **D)** NBS 4.3 with Vicra. Marker coordinates correspond to the crossing wires in the acrylic phantom assessed with the tracking device probe during neuronavigation. Colors indicate the average accuracy error across the three repetitions computed for each marker in the phantom. Red crosses represent the location of selected fiducial points.

Accuracy error differed between navigation systems, revealing a slightly lower error for NBS systems compared to InVesalius with MTC and Patriot ( $F_{3,1932} = 70.48$ ;  $p < 0.001$ ). Post hoc multiple comparisons indicated that mean accuracy error for NBS 3.2 with Spectra was 0.34 and 0.40 mm lower than for InVesalius with MTC and Patriot, respectively. Additionally, NBS 4.3 with Vicra accuracy error was 0.29 and 0.35 mm lower than for InVesalius with MTC and Patriot, respectively. No relevant differences were identified between InVesalius with MTC and Patriot, and no difference between NBS 3.2 with Spectra and NBS 4.3 with Vicra. Boxplot of accuracy errors for each system is depicted in Figure 2.5.

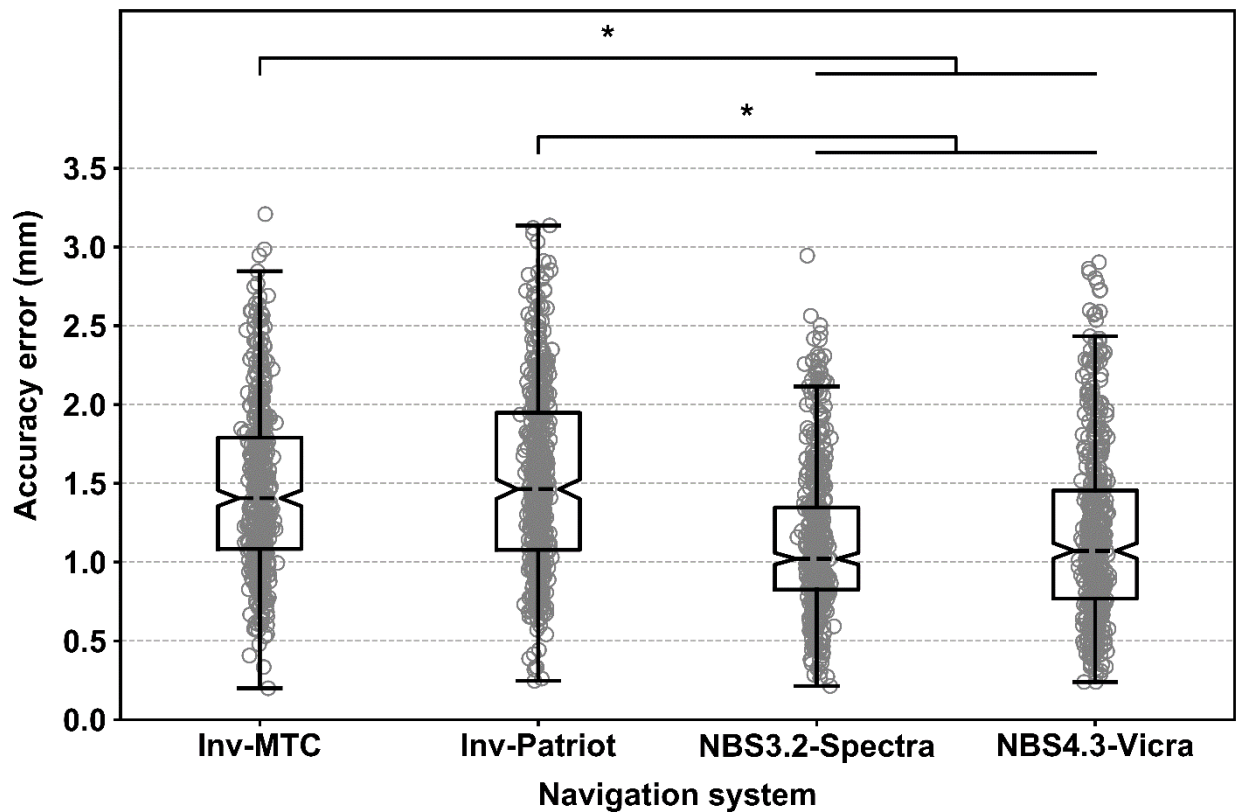


**Figure 2.5:** Measurements of accuracy error of InVesalius Navigator with MTC (Inv-MTC) and Patriot (Inv-Patriot), and NBS 3.2 with Spectra (NBS3.2-Spectra) and NBS 4.3 with Vicra (NBS4.3-Vicra). \*  $p < 0.05$

## 2.4.2 Control of coil position and orientation

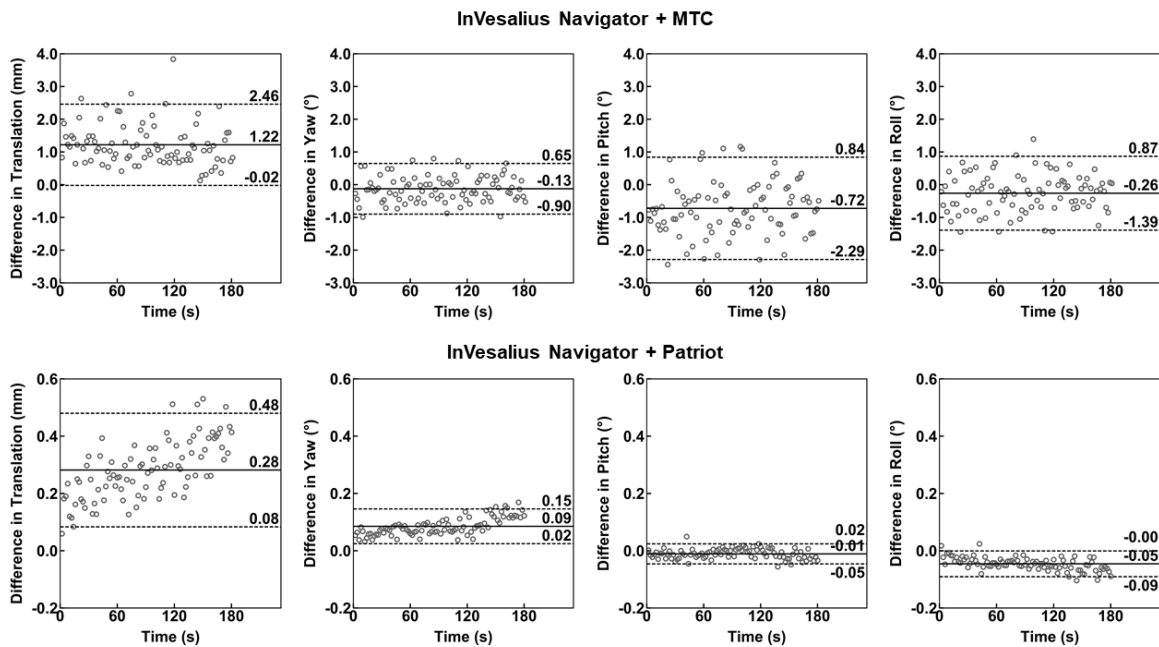
The repeatability and percentage of study variation (%StudyVar) resulting from the Gage R & R study are described in Table 2.2 for InVesalius Navigator with MTC and Patriot. The InVesalius measurements in a Gage R & R study are accurate if the contribution of the gage variability to the total study variability is lower than 10%. If the contribution is between 10 and 30%, the system is considered acceptable. For values greater than 30% the measurement is not accurate. Repeatability of InVesalius with MTC translation and InVesalius with Patriot pitch showed inaccurate measurements. In turn, all other measurements were either accurate or acceptable. Standard deviations of repeatability were lower than 1 mm or 1°, except for translation in InVesalius with MTC.

Figure 2.6 illustrates the difference of translation vector and rotation angles from targets recorded for 180 seconds with the TMS coil and the dummy head fixed. Largest ranges were obtained for translation with an upper limit of 2.46 mm and pitch with a lower limit of -2.29°, both for InVesalius with MTC. All values were lower than 3 mm or 3°, except for one sample of translation in InVesalius with MTC (3.83 mm).

**Table 2.2:** Repeatability as standard deviations and %StudyVar estimated in a Gage R & R study.

System Repeatability	Translation (mm) / %StudyVar	Yaw (°) / %StudyVar	Pitch (°) / %StudyVar	Roll (°) / %StudyVar
Inv-MTC	1.12 / 36.4% †	0.92 / 2.3%	0.97 / 29.9%	0.86 / 18.1%
Inv-Patriot	0.75 / 20.5%	0.42 / 1.37%	0.50 / 64.1% †	0.62 / 22.2%

† Represents %StudyVar higher than 30%.



**Figure 2.6:** Difference between measurements of translation and rotation angles (yaw, pitch, and roll) to target during navigation with InVesalius Navigator connected to MTC and Patriot. The solid line represents the average, and dashed lines the 1.96 times the standard deviation (95% intervals) for each coordinate.

### 2.4.3 Accuracy for revisiting a target

In the TMS experiment, difference to target varied between the coordinates of interest ( $F_{3,952} = 210.76$ ;  $p < 0.001$ ) and for the interaction effect of coordinate and tracking device ( $F_{3,952} = 6.24$ ;  $p < 0.001$ ). However, no significant effect of tracking device on the difference of measurements to target was found ( $F_{1,952} = 2.84$ ;  $p = 0.092$ ). Post hoc multiple comparisons revealed a significant variation of  $0.44^\circ$  in pitch between InVesalius with Patriot and MTC ( $p$

= 0.005). Figure 2.7 illustrates the comparison between InVesalius Navigator and each tracking device, for all assessed coordinates.

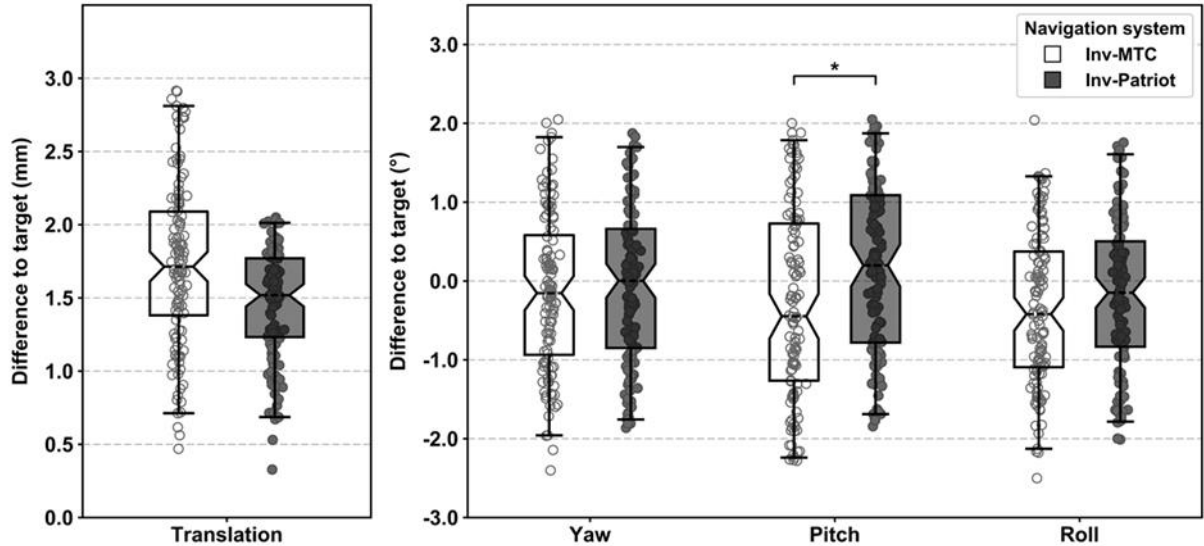


**Figure 2.7:** Difference to the target in translation and rotation angles (yaw, pitch, and roll) in the experiment of accuracy for revisiting a target with InVesalius Navigator connected to MTC (Inv-MTC; white boxes) and Patriot (Inv-Patriot; gray boxes). \*  $p = 0.005$

## 2.5 Discussion

In this chapter, we described the development of an open-source neuronavigation software compatible with multiple low-cost tracking devices and with specific tools for TMS experiments. Hereafter, we present an overview of the required pipeline and the general features of InVesalius Navigator. Our results indicate that registration and accuracy errors associated with the developed co-registration algorithm were low enough to provide good target localization and repeatability across multiple sessions. The overall accuracy and precision errors of the developed system are comparable to commercially available systems measured with a phantom and in a simulated TMS experiment.

### 2.5.1 Navigation pipeline and general features

Pipeline to work with InVesalius Navigator was designed to provide an intuitive flow of the navigation procedure. In general, neuronavigation can be started in five steps. First, the user imports the subject MRI or CT image set. Next, select the volumetric reconstruction in ray

casting or surface mode. Surface mode requires segmenting the mask with watershed and region growing algorithms. Both visualization modes provide the required anatomical insight of cerebral cortex to target the region of interest and fulfill the needs for navigated TMS.

In the third step, the user must select the desired spatial tracking device and register the desired object using the tracking probe. Then, select three fiducials in the image and record the same three fiducials coordinates using the tracking device probe. Finally, the user must click on Navigate button, and navigation procedure will start. During the navigation, it is possible to create spherical markers for reference in the 3D volume. Marker creation can be done by clicking on the correspondent button or by external trigger monitoring. The latter was developed for communicating with TMS devices and automatically create the marker in positions where pulses were applied. In addition, the user can define a marker as a target and enable an interface to guide the positioning of an instrument within a user-defined range of acceptance in translation and rotation angles. The target interface enables multi-session reliability of instruments positioning in several applications, such as navigated TMS.

InVesalius Navigator stands out in comparison with commercially available navigation system by being able to communicate with several spatial tracking devices, by its portability and minimum operational requirements. The software also provides methods for image and data manipulation, such as segmentation and processing tools. InVesalius Navigator stable version is distributed as an executable file that allows Windows (Microsoft Corporation) end users to easily install it [<https://www.cti.gov.br/invesalius>]. The source code with instructions for developers is hosted in a GitHub repository for version control [<https://github.com/invesalius/invesalius3>], and to allow third-party contributors to incorporate features relevant for their applications. The software runs on personal computers and laptops with at least 4 GB of RAM, multi-core processors with 2.0 GHz and 300 MB of hard-disk drive free space for installation. Graphics cards are not mandatory but may significantly increase 3D rendering quality and speed. InVesalius also can take advantage of GPU processing to optimize rendering.

### **2.5.2 Software validation**

InVesalius Navigator and NBS systems showed an FRE below 1 mm for all runs of measurements. The obtained values are in the range of those reported in the literature for several navigation systems (Kuehn et al., 2008; Omara et al., 2014; Ruohonen and Karhu, 2010). Even though the FRE is primarily used to indicate the accuracy of the navigation procedure its

interpretation is limited to the quality of registration procedure and fiducial points (Fitzpatrick et al., 1998). Therefore, maintaining a low FRE may prevent error propagation throughout the navigation procedure. The obtained FRE for InVesalius Navigator below 0.5 mm suggests that the proposed three-point fiducial co-registration algorithm is suitable for neuronavigation.

To assess the specific error to locate a target point in space, the TRE was estimated for all crossing points of the phantom considering each navigation system maximum FRE. Maximum estimated TRE was about 1 mm for all tested devices, except for NBS 4.3 with Vicra. The highest TRE for NBS 4.3 is probably due to the substantial maximum FRE compared to other systems. This observation highlights the importance of careful selection of fiducials, once larger registration errors may enhance the accuracy to locate a point in space. Figure 2.3 illustrates the spatial distribution of TRE for all points measured in the phantom. Points close to the centroid of fiducials configuration showed the lowest TRE while points with highest TRE were located opposite to the plane containing the fiducials. This observation corroborates the theory of TRE proposed by Fitzpatrick and colleagues (1998), pointing that the region of lowest TRE is close to the principal axis of the point set used for co-registration. Even though the TRE may be reduced for co-registration algorithms with higher number of fiducial markers, the estimated location errors seem to be low enough to provide accurate navigation.

The accuracy and precision errors obtained for all tested navigation systems are lower than the recommended limits for frameless systems, 2-3 mm for mean accuracy error (Orringer et al., 2012; Steinmeier et al., 2000) and 3-4 mm for 95<sup>th</sup> percentile (Mascott, 2006; Poggi et al., 2003), and lower than frame-based systems with 95<sup>th</sup> percentile of 3 to 5 mm (Maciunas et al., 1992). Moreover, NBS systems showed lower accuracy error of about 0.4 mm compared to InVesalius Navigator. The lower error for NBS systems is probably explained by the infrared optical tracking technology of Spectra and Vicra devices, which have been shown to provide excellent navigation accuracy in several commercial systems. However, in the applications of interest for InVesalius Navigator the error difference between NBS and InVesalius Navigator might be negligible as the mean accuracy for all systems were about 1.5 mm, half of the maximum recommended in the literature (Ruohonen and Karhu, 2010; Steinmeier et al., 2000).

Accuracy error spatial distribution showed lower values around the top part of the phantom and higher error on the bottom-most region, shown in Figure 2.4. Possible explanations to the accuracy error inhomogeneous spatial variation are the difficulty in accessing the points in the phantom and spatial inhomogeneity in co-registration error. To access all the points in the phantom required different probe entry maneuvers. Central, anterior and posterior areas were easily accessible while the top and bottom points were accessed with

increased difficulty, mainly because it required the probe to pass through the entire network of crossing nylon lines. This issue possibly led to an increase in the obtained accuracy error. Another possible explanation is that the target error given by the co-registration algorithm depends on the distance from the fiducial points centroid (Fitzpatrick et al., 1998). The region around the centroid showed the lowest TRE while the most distant corners resulted in the highest errors, thus affecting the accuracy error depending on the spatial location of each point.

The main factors influencing the neuronavigation accuracy are co-registration method, tracking devices technical specifications, image parameters and clinical events (Steinmeier et al., 2000). The phantom built for this study enabled assessment of the first two factors and our results indicate that errors associated to our system are comparable to those of commercially available devices (Steinmeier et al., 2000). Imaging geometric distortions might be disregarded in our study because the phantom tomographic image was created using a computational algorithm. Moreover, MRI distortions have already been shown to have a low effect on the navigation accuracy. In addition, clinical events that may arise from the brain and positional shifts during the procedure may also have minimal impact on non-invasive applications such as a TMS experiment.

It should be noticed that the position of the phantom points may vary due to the nylon wires flexibility. Therefore, it possibly overestimates the error of the navigation system if compared to other rigid phantoms. However, the flexible material was employed to allow the probe insertion through the phantom and to access the internal points. Moreover, the dimensions approximating a human head provided an overall visualization of errors spatial distribution relative to the fiducials markers. Considering that localization error is unevenly distributed in space, the development of a phantom with realistic head geometry would be an essential improvement to provide the assessment of errors with anatomical references.

### **2.5.3 InVesalius Navigator for coil positioning**

MTC and Patriot devices connected to InVesalius provided stable measurements of position and orientation during a 3-minutes recording, shown in Figure 2.6. Coordinates did not exceed the acceptance range of 3 mm or 3°. Interestingly, fluctuations of measurements with Patriot were lower than 0.5 mm in every coordinate, with maximum fluctuation in translation. Moreover, InVesalius Navigator with MTC showed larger variations than with Patriot, with larger variations in translation and pitch of about 2.5 mm and 2.3°, respectively. The larger variations in translation compared to other coordinates is possibly explained by the fact that it

sums x, y and z coordinates, and thus might be more sensitive to fluctuations in measurements from tracking devices. Overall, the apparent reduced stability of MTC compared to Patriot might be due to a more complex set of factors influencing the visible light camera-based algorithm compared to the electromagnetic measurement given by Patriot. The quality of navigation with MTC might be improved by using a different set of sensors and better room lightning.

Assessment of the TMS coil position and orientation across distinct registrations revealed an excellent level of repeatability, below 1 mm or 1°, in all coordinates for InVesalius with MTC and Patriot, except translation in InVesalius with MTC. Gage R & R study showed a high variability of translation in InVesalius with MTC and pitch in InVesalius with Patriot. However, the repeatability is lower than the tolerance accepted for neuronavigation and might not significantly affect the navigation accuracy. The increased variability in translation for InVesalius with MTC is probably explained by the lower measurement stability discussed in the previous paragraph. Also, optical markers attached to the TMS coil in this experiment were relatively small compared to the camera-sensor distance during navigation. Possibly, the repeatability and stability of measurements with MTC can be improved by designing suitable, larger optical markers for better acquisition of coordinates with the camera. Nevertheless, the registration algorithm of InVesalius Navigator provided accurate, i.e. below 3 mm or 3°, measurements of coil position and orientation within multiple combinations of head and object registrations with both tracking devices.

Finally, in the target revisiting experiment both tracking devices allowed the object placement within a difference of 3 mm or 3° over the stimulation target. Moreover, the interface to guide the TMS coil positioning provided accurate return to the stimulation target across different objects and head co-registrations. The difference in pitch angle varied between InVesalius with MTC and with Patriot. Ambrosini et al. (2018) also reported a difference in positioning of the pitch angle between StimTrack and BrainSight (Rogue Research Inc., Montreal, Canada). Considering that pitch is the elevation angle that moves the tracking sensor attached to the object farther away from the plane of the camera, there might be a decrease in measurement agreement in this specific coordinate. Patriot seems to be less affected in this specific orientation and might provide a better estimate, due to the spherical symmetry of the electromagnetic field used to measure the coordinates. Also, the elevation angle is aligned with the direction of the force applied by the handle to support the coil's weight. Therefore, a greater variation might be expected in this orientation in which the balance of forces is more critical.

In this case, the use of a navigated guiding interface might be of utmost importance to reduce the variability of TMS coil positioning across multiple sessions.

## **2.6 Conclusion**

Our study showed that InVesalius Navigator connected to either MTC or Patriot provide accurate neuronavigation within the acceptance range discussed in the literature. The errors are comparable to those of commercial system. Finally, InVesalius Navigator is the first image-guided open-source and free navigation software for TMS coil positioning and might be useful to improve the reliability of physiological experiments across different research and clinical centers.

# 3. Neuronavigation and patient-specific models

---

## 3.1 Introduction

In this study, we developed patient-specific models for neurosurgical planning using 3D printing. Furthermore, we assessed the accuracy of performing measurements with a neuronavigation system. Lastly, as an attempt to optimize time and total cost of production, we investigated the effects of scale reduction on a patient-specific model printed in three different sizes.

## 3.2 Material and methods

### 3.2.1 Patient-specific models

Two 3 year-old boys, one diagnosed with refractory epilepsy on the right temporal lobe and other with Sturge-Weber syndrome were selected to participate in this study. Hereafter, models produced for each subject are named as S1 and S2, respectively. The Hospital das Clínicas da Faculdade de Medicina de Ribeirão Preto ethics committee approved the experimental procedure, and the responsible person gave informed signed consent (CAAE 36460914.4.0000.5440).

Volumetric brain MRIs were acquired by an Achieva 3T scan (Philips). Images were segmented to reveal the cortical surface and a representative portion of each patient's face. The 3D models were reconstructed and exported to stereolithography file (.STL) using the InVesalius software. Models S1 and S2 were produced in the original size of each patient by selective laser sintering of polyamide in a Paragon 3D printer (Paragon Rapid Technologies, Darlington, UK). Model S2 with real size was named as B100.

Model S2 was printed in two additional sizes for assessment of the scaling effects. First, a model with half of the original size (B50) was printed by extrusion of polylactic acid (PLA) in a ZMorph 2.0 SX (ZMorph, Wrocław, Poland) – total printing time approximately ten hours. Finally, a model with one-quarter of the original size (B25) was printed in a Prusa i3 (Rep Rap, Beijing, China) with PLA extrusion – total printing time of approximately 3 hours. Both models were printed using a layer thickness of 0.1 mm.

### 3.2.2 Errors of neuronavigation in patient-specific models

The error of measurements during neuronavigation inside the brain was assessed with model S1. Four holes were perforated in the solid brain model using a surgical drill. Each hole had depths of  $54.0 \pm 0.5$ ,  $43.0 \pm 0.5$ ,  $43.0 \pm 0.5$  and  $23.0 \pm 0.5$  mm, indicated by the numbers 1, 2, 3 and 4 in Figure 3.1, respectively. The distance between the top and bottom edges of each hole was measured using a ruler and during neuronavigation, with the probe of MTC device connected to InVesalius Navigator.

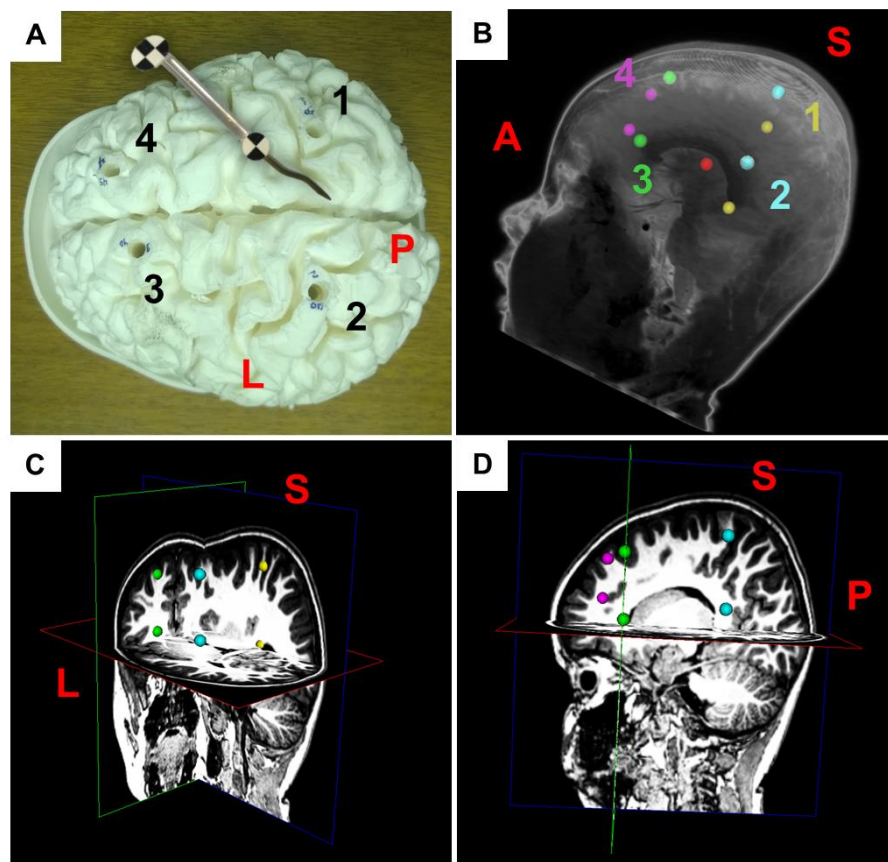


**Figure 3.1:** A) 3D printed S1 model with the tracking probe of MTC. B) Neuronavigation markers are indicating top and bottom coordinates of each hole. C) Neuronavigation markers on three orthogonal planes and on D) sagittal plane view.

Model S2 was employed to estimate the errors associated to neuronavigation in brain and head surface (Figure 3.2A). We assessed the anterior-posterior length in left (AP-LH) and right hemispheres (AP-RH), the distance between right and left ears (RL ears) and the lengths of insula (r-insula), cuneus (r-cuneus) and prefrontal cortex (r-prefrontal) in the right hemisphere. Figure 3.2B shows each recorded pair of landmarks. Three measurement modalities were used,

an analogic caliper, the ruler function in InVesalius software 3D viewport and the marker creation function of InVesalius during neuronavigation with Patriot. Two independent evaluators performed the entire procedure. The coefficient of variation (CV) was computed as the ratio between the standard deviation and the average across measurements modalities and evaluators. Lastly, the quality of the co-registration was visually inspected using a point cloud scanned over the entire perimeter of the scalp (Figure 3.2C) and by markers created along the anterior gyrus of the primary motor cortex (Figure 3.2D).

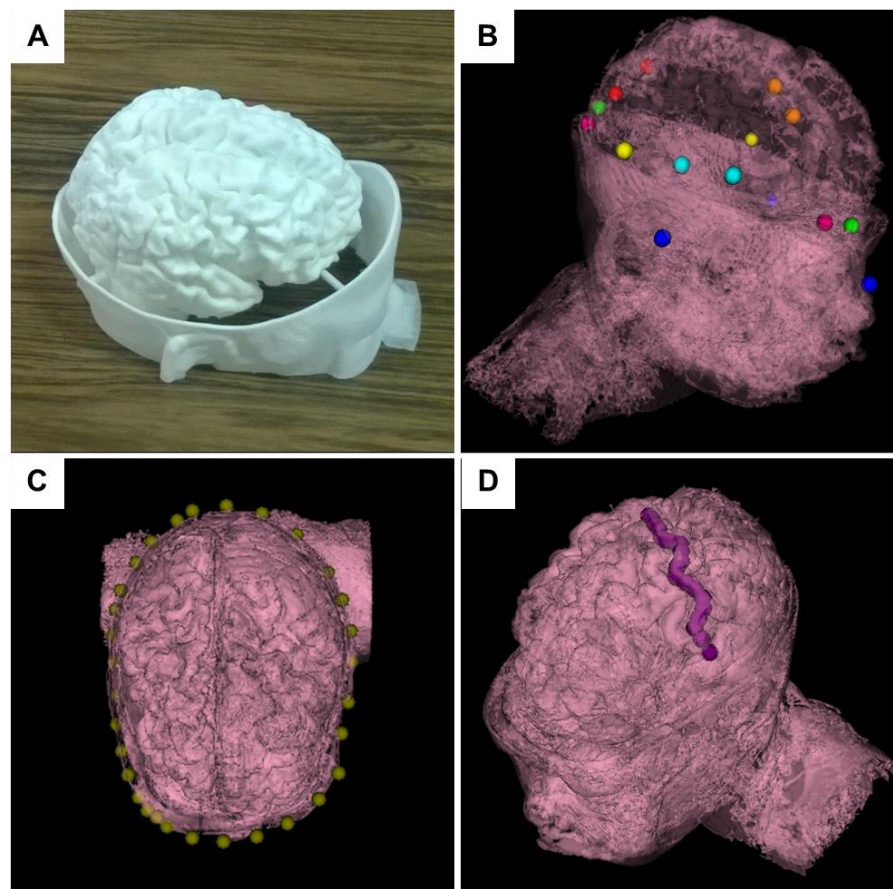


**Figure 3.2:** **A)** 3D printed model S2. **B)** Fiducial points (dark blue) and landmarks in the InVesalius volumetric view. Two markers representing one anatomical landmark are represented with the same color. AP-LH (green), AP-RH (pink), RL ears (dark blue), r-insula (cyan), r-cuneus (red) and r-prefrontal (orange). **C)** Markers were created during neuronavigation surrounding the perimeter of the head model and **D)** along the posterior gyrus of the central sulcus, for assessment of co-registration quality.

### 3.2.3 Scaling effects on patient-specific models

Scaled models and neuronavigation were used to assess the effects of scale reduction on neuroanatomical localization. Navigation was performed using the InVesalius Navigator connected to the optical tracking device MTC. Image registration was performed using point-based registration and linearly adjusted to the corresponding scale factor. FRE was calculated for each procedure as a control for navigation quality. The coordinates of nine anatomical landmarks of clinical relevance were digitized during neuronavigation for each model (Figure 3.3): left (LE) and right ears (RE), LE and nasion (N), RE and N, left (LPC) and right parietal cortex (RPC), left (LFC) and right inferior frontal cortex (RFC), and left (LOC) and right inferior occipital cortex (ROC).

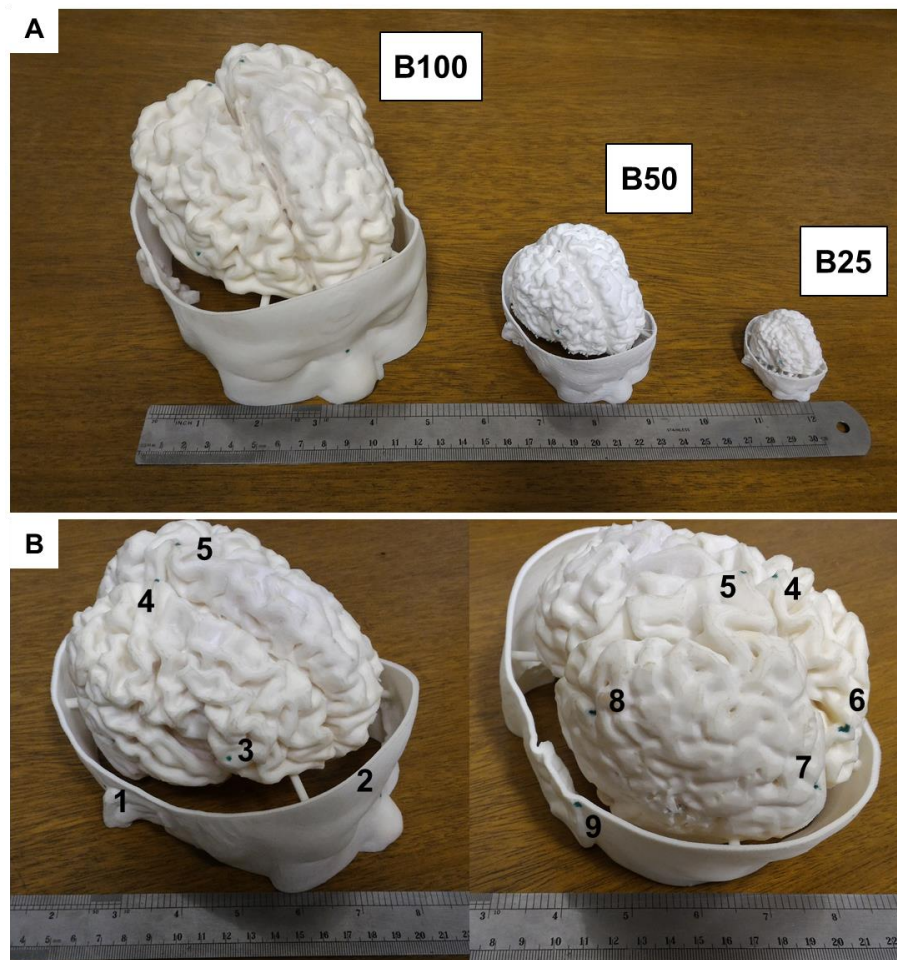


**Figure 3.3:** 3D printed scaled models of S2 and anatomical landmarks. **A)** Real size B100, half-sized (B50) and quarter-sized (B25) models. **B)** Frontal and back view of anatomical landmarks used for navigation and measurements: 1. RE, 2. N, 3. RFC, 4. RPC, 5. LPC, 6. ROC, 7. LOC, 8. LFC and 9. LE.

### 3.2.3.1 Statistical analysis

Euclidian distances between the six pairs of digitized landmarks were calculated (LE-N, LE-RE, RE-N, LPC-RPC, LFC-RFC, LOC-ROC). Two-way ANOVA was used to test if measured distance depends on both the scale factor and target pair of anatomical landmarks. Post hoc Tukey's test was used for multiple comparisons and the level of statistical significance was set at 5%.

## 3.3 Results

### 3.3.1 Errors of neuronavigation in patient-specific models

The differences between measurements with the ruler and the neuronavigation system inside the brain are shown in Table 3.1. The average difference  $\pm$  standard deviation between both methods was  $1.4 \pm 1.1$  mm.

**Table 3.1:** Measurements of distance between surface and bottom of each hole in the brain model.

	Hole 1	Hole 2	Hole 3	Hole 4
<b>Ruler (mm)</b>	54.00	43.0	43.0	23.0
<b>Neuronavigation (mm)</b>	55.1	42.9	40.4	25.0
<b>Difference (mm)</b>	1.1	0.1	2.6	2.0

Regarding the measurements of anatomical landmarks in model S2, more distant reference points, such as AP-LH, AP-RH, RL ears presented a mean CV of 1.43%. Meanwhile, shorter distances, like the r-insula, r-cuneus and r-prefrontal presented an average CV of 12.90%. The distance measurements for all anatomical references and correspondent assessment methods are displayed in Table 3.2.

**Table 3.2:** Euclidean distance of anatomical landmarks estimated by one rater in InVesalius interface, with a caliper and during navigation (Navigation 1), and by a second rater only during navigation (Navigation 2).

	<b>InVesalius</b> $\pm 0.01$ mm	<b>Caliper</b> $\pm 0.05$ mm	<b>Navigation 1</b> $\pm 0.01$ mm	<b>Navigation 2</b> $\pm 0.01$ mm	<b>CV</b> (%)
<b>AP RH</b>	133.00	133.00	132.00	134.00	0.61
<b>AP LH</b>	148.53	152.00	147.50	148.90	1.63
<b>r-insula</b>	22.87	19.75	24.44	29.70	10.35
<b>r-cuneus</b>	23.30	21.05	23.69	13.34	7.17
<b>r-prefrontal</b>	12.28	9.08	15.47	12.55	21.19
<b>RL ears</b>	107.14	110.30	114.21	122.77	2.06

### 3.3.2 Scaling effects on patient-specific models

Estimated FRE for neuronavigation (mean  $\pm$  standard deviation) was  $2.5 \pm 0.3$  mm for B25,  $1.7 \pm 0.2$  mm for B50 and  $1.5 \pm 0.3$  mm for B100. Two-way ANOVA revealed that calculated distance depends on both scale factor ( $F_{2,144} = 40.56$ ;  $p < 0.001$ ) and pair of anatomical landmarks ( $F_{5,144} = 55951.70$ ;  $p < 0.001$ ). Also, a significant interaction was found between the pair of fiducial coordinates and scale factor ( $F_{10,144} = 11.78$ ;  $p < 0.001$ ). Multiple comparison tests revealed that LE-RE distance was greater in B25 compared to B50 and B100 (95% confidence interval 125.8 – 129.6;  $p < 0.001$ ). Difference between LE-RE in B25 and B50 was 2.6 mm, and B25 and B100 was 2.7 mm. The distance between RE-N was greater for B25 than B50 and B100 (95% confidence interval 124.0 – 127.8;  $p < 0.001$ ), mean differences were 5.8 mm and 5.1 mm, respectively. Remaining pairs of anatomical landmarks did not show any statistical difference between models of different scales. In general, distance measurements showed a tendency for higher deviations on the smallest model then for B50 and B100 (Figure 3.4).

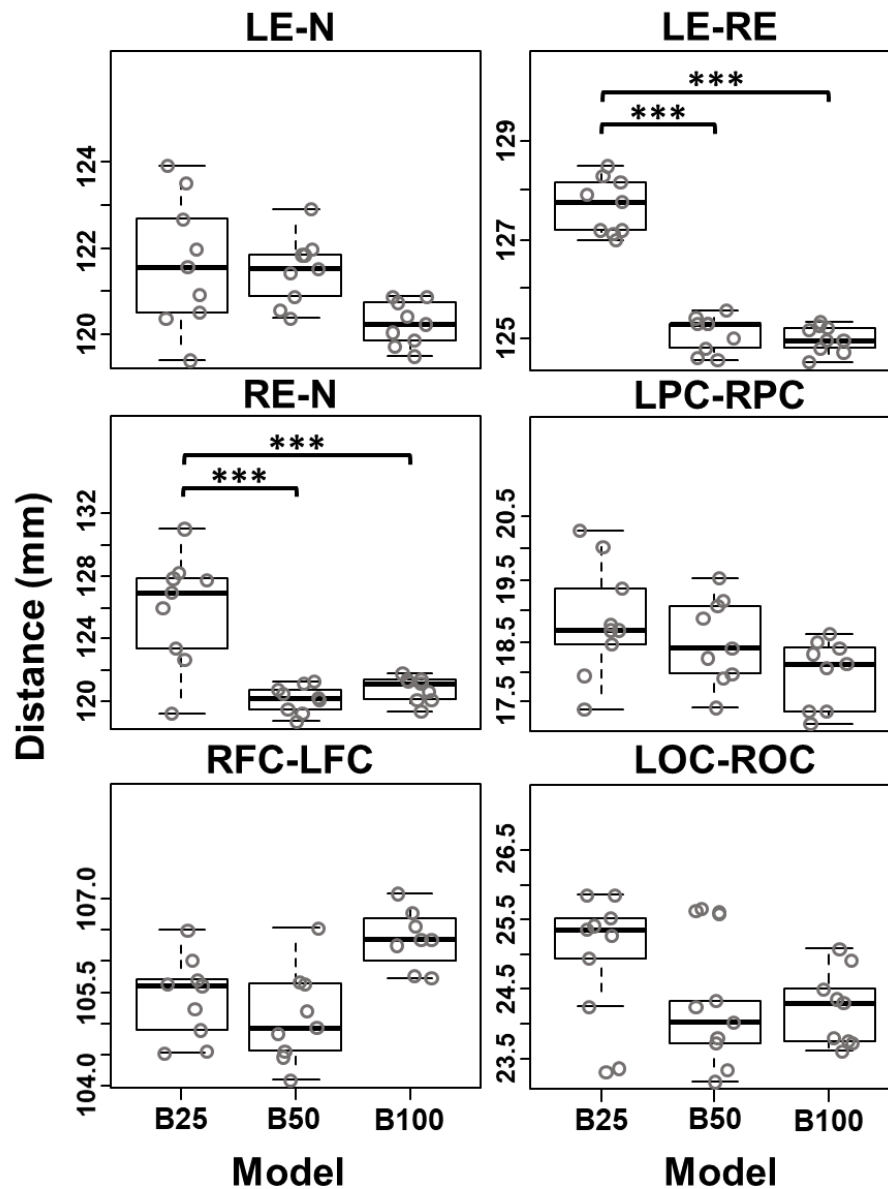


**Figure 3.4:** Boxplot of the distance measured on the six pairs of anatomical landmarks in each scaled model. LE-RE and RE-N showed higher distance values when measured in B25 compared to B50 and B100. \*\*\*  $p < 0.001$

### 3.4 Discussion

Models from S1 and S2 offered a strong, vivid visual impression, and its quality allowed identification of landmarks and successful navigation across brain structures. The potential to grasp and inspect details of the actual anatomy can aid surgeons to plan complex operations, aiming better patient prognosis. Furthermore, the InVesalius Navigator software enabled real-time localization and digitization of anatomical structures with measurement errors within

limits provided by literature for clinical practice, i. e., below 3 mm (Kuehn et al., 2008; Omara et al., 2014). The combined use of 3D-printed models and neuronavigation might allow practicing and simulation of the whole surgical procedure in advance. Such a strategy would probably increase the confidence of the entire clinical team during the actual procedure (Gasco et al., 2013).

Inspection of model B50 printed with PLA and model B100 manufactured with selective laser sintering provided a quantitative and realistic visual analysis of patient's cortical anatomy, without distortion caused by scale reduction. However, reduction into one-quarter of the original size smoothed the surface details, hindering the identification of anatomical landmarks. Reducing the model's size drastically decreased printing time. Model B25 took three hours of total printing time, B50 ten hours and model B100 twenty-four hours. Even though a comparison of printing times is biased by using different printers for scaled models, it might provide an overall idea of the time needed for the production of each method.

Neuronavigation on B50 and B100 provided more accurate and precise distance measurements than on model B25. The smallest model showed higher measurements deviations, specifically for LE-RE and RE-N. Both pairs of anatomical landmarks had the right ear as one of the references, suggesting that a possible systematic deviation is associated with the acquisition of the coordinates in the B25 model. Indeed, it was expected that B25 had lower quality results when compared to B50 and B100, once the small size approximates all measurements to the uncertainty levels. Moreover, none of the remaining references showed any difference associated with distance measurements across scale factors. A possible explanation may be the difficulty on visually localizing the same reference points on the smallest model compared to the larger ones. We should highlight that B50 had enough precision for simulation proposes. Reducing the scale for printed models without quality loss may help to reduce the time spent and cost of producing models. Thus, neuronavigation with B50 may be a suitable alternative to the real size model with similar visual detailing (Grillo et al., 2018).

Our procedure has some technical limitations. First, the anatomical landmarks were selected by non-medical professionals, and this may have introduced an additional source of errors. Also, the number of patients was small, which might limit the interpretation of our findings. For a future study, we should assess the accuracy error of neuronavigation studying more parameters that might affect the quality of 3D-printed models, such as printing layer thickness, MRI resolution, and infill ratio.

### **3.5 Conclusion**

This chapter introduced the possible combination of neuronavigation and 3D-printed models for neurosurgical planning. Our study suggests that patient-specific models provide sufficient detail of neuroanatomical structures and might be a useful tool in clinical routine. Furthermore, the evaluation of multiscale models might be a successful alternative to improve time and evaluate general steps of surgical procedures. Finally, the combined use of neuronavigation with 3D-printed models is a candidate for the practice of surgical maneuvers before the actual procedure.

# 4. TMS coil with electronic control of E-field orientation

---

## 4.1 Introduction

This chapter aimed to describe the optimization and manufacture of a multi-locus TMS (mTMS) coil to control the E-field orientation electronically without manual adjustments. Additionally, we aimed to investigate with high angular resolution how MEPs depend on the E-field orientation.

## 4.2 Material and methods

### 4.2.1 Optimization parameters

A mTMS coil was constructed with two superimposed orthogonal figure-of-eight coils to control electronically, i.e., without moving the stimulation coil, the induced E-field orientation. The coil was manufactured in two steps. First, current loops were computed using an optimization procedure for minimum-energy coils, as proposed by Koponen et al. (2017). Second, the wires were wound in a coil former designed and produced based on the computed current paths. Here, we provide a summary of the optimization method, and the reader is referred to the papers of Koponen et al. (2017, 2015) for the mathematical formulation. In this study, the optimization was performed using an octagonal plane geometry for the coil and a spherical shape to represent the cortical surface. The octagonal geometry was chosen due to its symmetry with respect to two Cartesian axes. Also, the spherical geometry approximates well the curvature of the primary motor cortex (Nummenmaa et al., 2013), which is reasonable for the aimed applications.

The optimization procedure calculates a set of current distributions in a plane capable of inducing a desired set of E-field distributions with constrained focality and intensity in a particular head geometry. The procedure minimizes the energy of the magnetic field generated by the set of current distributions when producing a stimulating E-field. Therefore, to solve the optimization problem, we needed to compute the coil magnetic field energy, the coil E-field distribution and the desired set of E-field distributions in different orientations.

The plane was discretized in a triangular mesh. Every small triangle has a magnetic moment generated by an elementary current loop surrounding each vertex in a given time

instant. The magnetic field energy was taken as the cost function for optimization and was computed using a semi-analytical integration (Koponen et al., 2017). The resulting equation (Equation 4.1) is in quadratic form and can be solved by the interior-point method for convex optimization.

$$\mathbf{U} = \frac{1}{2} \mathbf{I}^T \mathbf{M} \mathbf{I} \quad (4.1)$$

where  $\mathbf{M}$  is the matrix of self- and mutual inductances and  $\mathbf{I}$  the current in all elementary loops of the coil. In turn, the E-field was computed by means of the reciprocity between magnetoencephalography and TMS, and boundary element methods (Nummenmaa et al., 2013). The constraints parameters applied for optimization were defined from the focality of desired E-field distribution induced by a conventional figure-of-eight coil, as described in Table 4.1. For the conventional coil, we considered the geometry of the commercial figure-of-eight Magstim 70 mm Double Coil (The Magstim Co Ltd, UK; Figure 4.1A) (Thielscher and Kammer, 2002). The lead-field matrix containing the E-field distribution at all possible points in the spherical cortical surface was determined by the rate of change of the magnetic moment density in each triangle of the coil. The result was a set of surface current distributions that generates the desired E-field in each target orientation.

Regarding the E-field distribution, the focality was determined as the full-width at half-maximum (FWHM) values in the area that the E-field norm is higher than 70% of the maximum, i.e., 50% of the maximum energy density (Koponen et al., 2015).

**Table 4.1:** Constraints used for the coil optimization, adapted from Koponen et al. (2015, 2017).  $E_{\parallel,0}$  and  $E_{\perp,0}$  are the parallel and perpendicular components of induced E-field at the focal point.

<b>Equality constraints</b>	$E_{\parallel,0} = 100 \text{ V/m}$	at the focal point
	$E_{\perp,0} = 0$	at the focal point
<b>Inequality constraints</b>	$ \mathbf{E}  \leq  \mathbf{E}_0 $	everywhere
	$ \mathbf{E}  \leq  \mathbf{E}_0 /\sqrt{2}$	outside the focal region

The next step consisted of finding the linear combination of all possible solutions of the optimization that can induce the E-field distributions in all desired orientations. Each component in the linear combination can be considered as a single coil. A matrix factorization using the singular value decomposition method was applied to select the essential components.

To rotate the E-field around the normal direction of the coil is a problem with one degree of freedom, and therefore two orthogonal components are the expected solution, Figure 4.1B. After decomposition, the contour lines of the current distribution stream function were computed to obtain the paths for the coil windings, Figure 4.1C.

The optimization procedure was performed by adjusting several parameters to generate a practical TMS coil with dimensions suitable for stimulation of human primary motor cortex. The human cortex was modeled to be spherical with a radius of 70 mm (Koponen, 2013; Nieminen et al., 2015), and with a mesh with 2563 vertices. The packing of wires during manufacturing would move the top coil further away from the cortical surface. Thus, optimization was performed in two separate planes to compensate for the possible difference in current intensity needed to generate the same E-field. Bottom and top plane coils were positioned tangentially, at 15 and 20 mm from the cortical surface, respectively.

To find the optimal size and number of turns, we changed the outer diameter of the octagonal plane from 11 to 19 cm, in steps of 2 cm. The total number of turns in both windings ranged from 10 to 16, in steps of 2. The target E-field from the conventional coil was generated from 0 to 180° in steps of 10°. We also ran the optimization using a target E-field generated from 0 to 90° in steps of 1°, but there was no difference in estimated quantities. Parameters selected for optimization are shown c. The current necessary to induce an E-field of 100 V/m with a rise-time of 50  $\mu$ s, maximum energy, coil inductance and the minimum distance between the innermost loops were computed to estimate the optimal size and number of turns of the possible mTMS coil.

**Table 4.2:** Values tested for each parameter during coil optimization.

<b>Parameters</b>	<b>Values</b>
Coil diameter (cm)	11, 13, 15, 17, 19, 21
Number of turns	10, 12, 14, 16
Tested orientations	0 to 180° in steps of 10°

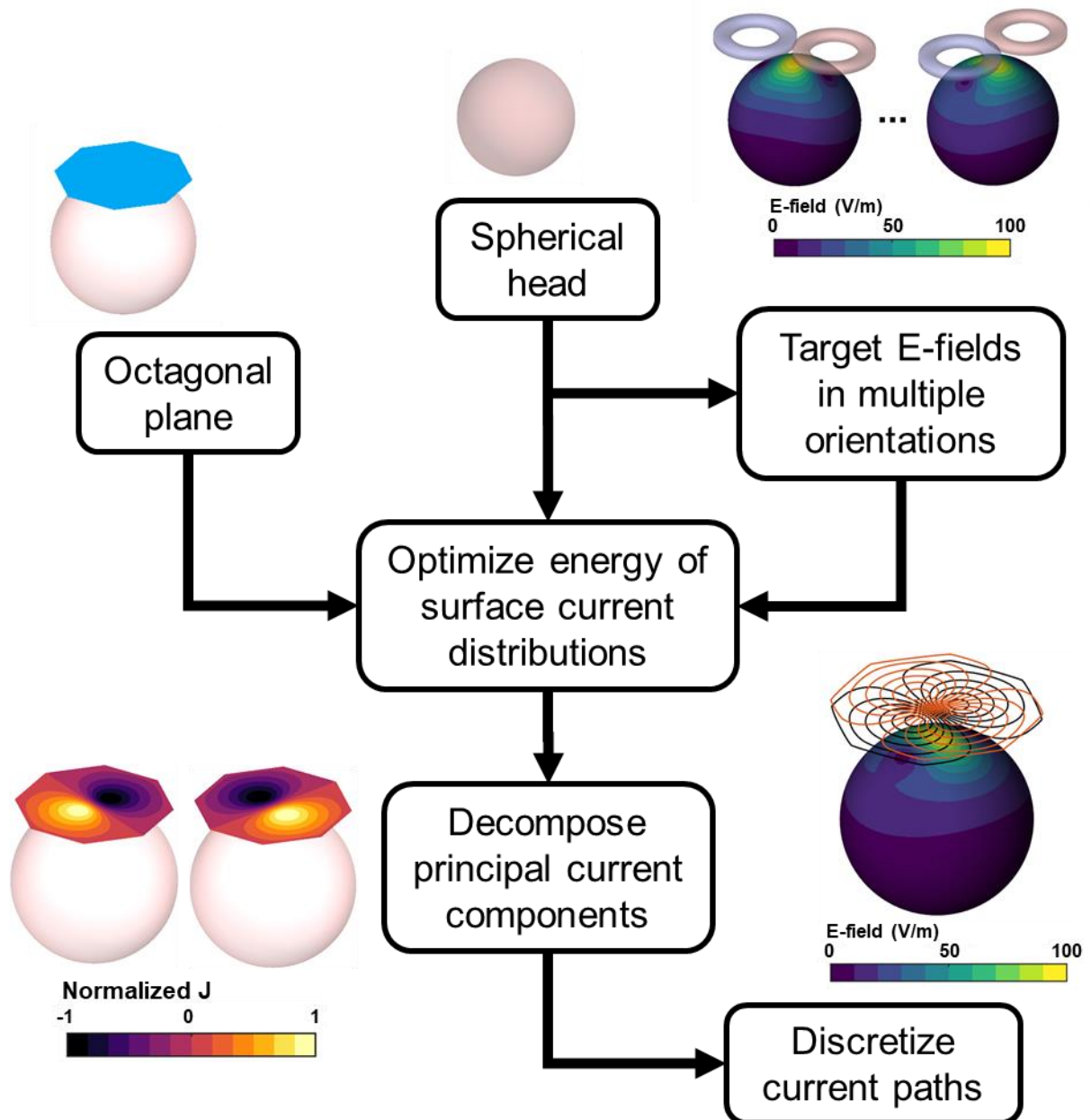


**Figure 4.1:** Pipeline followed to obtain the current paths for a minimum-energy mTMS coil with electronic control of E-field orientation. Optimization algorithm uses the E-field distribution induced by a conventional, figure-of-eight coil in a spherical head surface. The target E-field has peak intensity of 100 V/m and was rotated between 0 and 180°. The minimum-energy current distributions were computed with constraints given in Table 4.1, and based on the target E-fields. Surface current densities, denoted by  $\mathbf{J}$ , were decomposed in two components with orthogonal distributions to allow stimulation of E-field in any orientation parallel to the plane. Current values were normalized for visualization. Lastly, current distributions were discretized in 12 turns along the contour lines of its stream function. The resulting induced E-field has focality and distribution similar to that of the conventional figure-of-eight coil, but orientation can be adjusted by driving proportional currents in the top (solid orange lines) and bottom (solid black lines) paths.

## 4.2.2 Coil manufacturing and calibration

Two separate coil formers were designed using SolidWorks 2016 (Dassault Systèmes, Waltham, MA, USA), for the top and bottom coils, Figure 4.2A. Formers were printed by selective laser sintering of glass-filled polyamide (Maker 3D, Helsinki, Finland). Glass-filled polyamide has a tensile strength of 38 MPa and dielectric strength of 15 kV/mm, and are resistant to the pressure of about 10 MPa that results from Lorentz forces during the TMS pulse (Koponen, 2013). Each coil comprised of two layers in series of Litz wire (1.6 mm thick and 2.4 mm wide; Rudolf Pack GmbH & Co. KG, Gummersbach, Germany), glued to the former grooves and filled with epoxy. Also, there was a gap of 2 mm between the windings of the bottom and top coils that was filled with epoxy. Figure 4.2B shows the resulting coil windings and 3D-printed former.

The constructed coils' self-inductance and resistance were measured using a shunt resistor of  $99.3 \Omega$  connected in series to a sinewave generator and a digital oscilloscope. The frequencies of the sinewave were adjusted to 1, 2, 3, 5, 10, 20, 50 and 100 kHz. Self-inductance and the equivalent resistance of the coil were estimated using the phase difference of the voltage measurements.

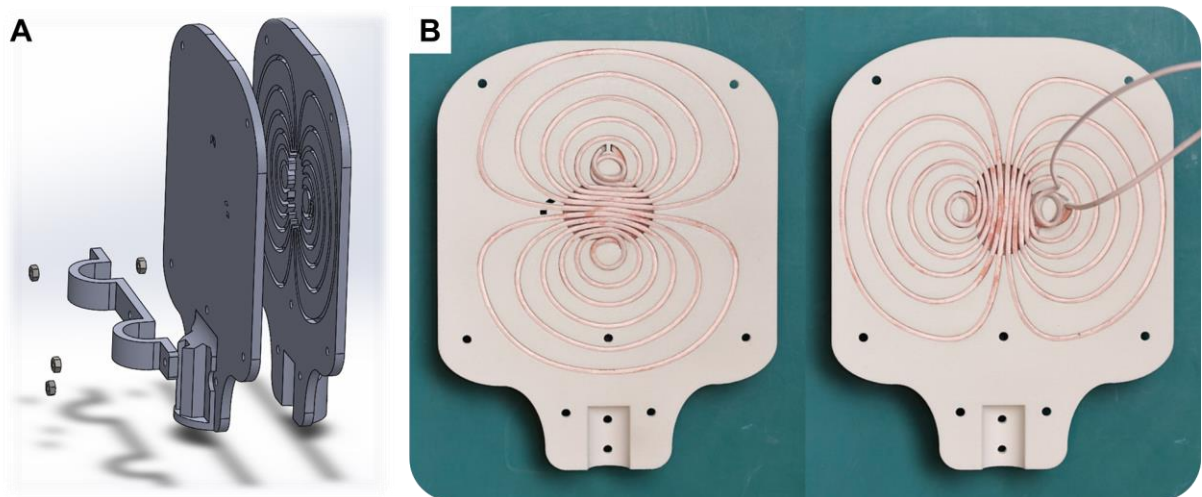


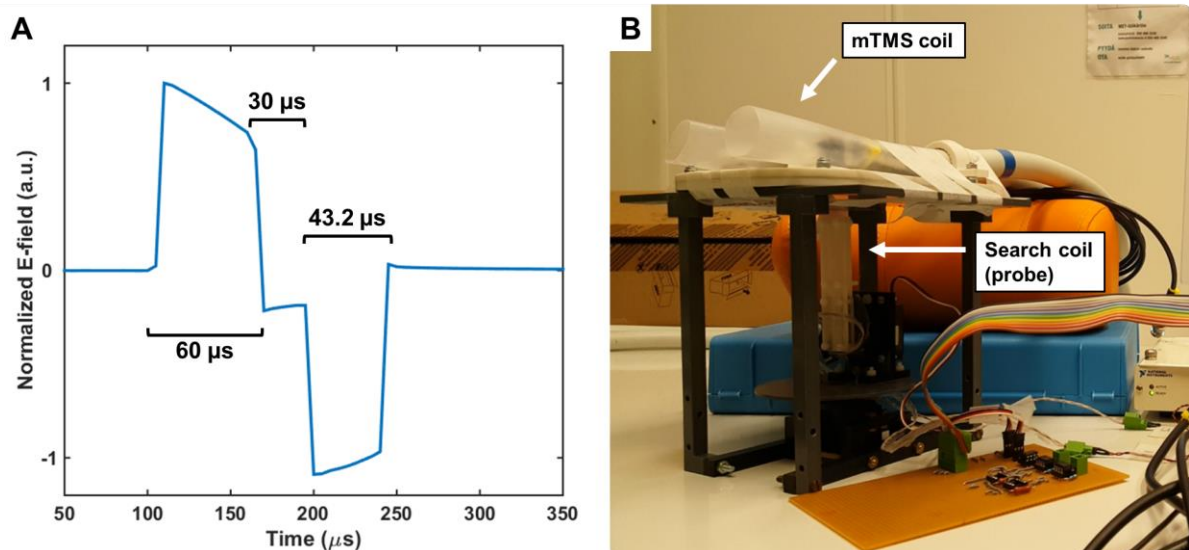
**Figure 4.2:** **A)** Virtual model of the designed coil formers. **B)** 3D-printed coil former with the copper wires wound in the top part (left) and bottom part (right).

Next, the coil was welded to commercial cables provided by Nexstim (Nexstim Plc), and attached to a custom-made mTMS device. The device delivered monophasic pulses through a circuit with four insulated-gate bipolar transistors (5SNA 1500E330305, ABB, Zurich, Switzerland) in a full-bridge configuration and a pulse capacitor (1020  $\mu\text{F}$ , E50.R34-105NT0,

### mTMS coil

Electronicon Kondensatoren GmbH, Gera, Germany). Two circuits were mounted to generate independent currents in the top and bottom coils. A capacitor charger (CCPF-1500-1.5P, Lumina Power, Inc., Bradford, MA, USA) and a resistive circuit are used to adjust capacitor voltages. The device is controlled by software written in LabVIEW, partially running on a field-programmable gate array (NI PXI-7841R, National Instruments, Austin, TX, USA). The monophasic pulse generates an E-field waveform with three plateaus lasting 60.0, 30.0 and 43.2  $\mu\text{s}$ , respectively positive, negative and negative, shown in Figure 4.3A. The duration of the last waveform plateau was adjusted to minimize the time needed for the E-field decay to return to zero. Otherwise, a slow decay might occur, leading to a prolonged plateau depending on E-field intensity.

The stimulator device was calibrated to allow electronic control of the E-field orientation by adjusting the voltages delivered in each channel of the coil. The E-field distribution was measured with a probe constructed in a triangular-based combination of two perpendicular search coils with 5-mm tangential and 70-mm radial lengths (Nieminen et al., 2015), shown in Figure 4.3B. The probe measures the induced electromotive force around a hemispherical shell, with position controlled by two servo motors. The coil was placed on the top of the device 15 mm from the tip of the probe, with initial orientation ( $\theta = 0^\circ$ ) representing the current flowing in posterior-anterior direction of the coil, and increasing in a clockwise direction. With the probe in the initial position, we searched for the capacitor voltage necessary to generate, separately, an E-field intensity of 25 V/m for the bottom coil in  $0^\circ$  and top coil in  $90^\circ$ . Next, we analytically derived the equation of the capacitor voltage in each coil to induce an E-field with norm  $|E|$  and orientation angle  $\theta$ .



mTMS coil

**Figure 4.3:** **A)** E-field waveform generated by a monophasic current pulse with 60- $\mu$ s rise-time, with adjusted timing parameters. **B)** Measurement set-up of E-field calibration. The probe has two orthogonal 5-mm wire paths on the tip and rotates around a hemisphere with 70-mm radius. For each position, measurement was performed in both directions to provide the distribution and orientation of the E-field.

Then, we measured with the probe the orientation and norm of the E-field with the capacitor voltage adjusted by the derived equations for E-field norm of 25 V/m and orientation ranging from 0 to 180° in steps of 15°. Experimental orientation and E-field intensity were computed with the resulting servo coordinates and induced an electromotive force in each component of the probe. To measure parallel and perpendicular components of the E-field FWHM, we swept the probe's  $\theta$  coordinate from  $-90^\circ$  to  $+90^\circ$ , stimulating with pulses at 300 V of capacitor charge for the bottom and 0 V to the top coil. Next, the same step was performed with 300 V applied to the top and 0 V to the bottom coil. Finally, we measured 1000 points around the entire hemisphere of the measurement device with TMS induced E-field at 25 V/m and orientation set to 0, 45 and 90°.

### 4.2.3 Assessment of motor cortex orientation-dependency

For experimental validation of the constructed coil, we assessed the primary motor cortex orientation dependency with high angular resolution. Thirteen healthy subjects (4 women;  $29.8 \pm 4.8$  years old), all asymptomatic to neurological and motor disorders, participated in this study after giving a written informed consent. The study was performed in accordance with the Declaration of Helsinki and approved by the Coordinating Ethics Committee of the Hospital District of Helsinki and Uusimaa.

Subjects sat comfortably in a reclining chair with arms and hands fully relaxed during the entire experiment. EMG was recorded from the right *abductor pollicis brevis* (APB) muscle using circular surface electrodes in a belly-tendon montage. The skin surface was cleaned with alcohol to reduce the electrode-skin impedance. Signals were recorded with the Nexstim eXimia EMG device (500-Hz low-pass filtering, 3000-Hz sampling frequency; Nexstim Plc). Before the TMS experiment, all subjects underwent an anatomical T1-weighted gradient echo MRI recording with voxel size of (1 x 1 x 1) mm. The MRI was used to monitor the coil orientation, position, and tilt using the NBS 3.2 neuronavigation system (Nexstim Plc). First, for each participant, the APB hotspot was identified as the cortical site beneath the coil center resulting in MEPs with maximum amplitude for a single TMS pulse. The search for the hotspot was performed along the central sulcus using an E-field of 60 V/m. Then, the resting motor

threshold was identified as the minimum stimulation intensity eliciting at least 10 out of 20 MEPs with amplitude higher than 50  $\mu\text{V}$  (Rossini et al., 2015). The hotspot and motor threshold were determined with coil orientation approximately perpendicular to the central sulcus, in a posterior-anterior direction, and approximately 45° to the midsagittal line (Kallioniemi et al., 2015a; Souza et al., 2017). Hereafter, we set the 0° as the orientation used to identify the hotspot and motor threshold.

Five single pulses at 110% of resting motor threshold were applied from 0 to 357° in steps of 3°, to build the amplitude-orientation curve. The intensity of 110% of resting motor threshold was selected to achieve better muscle selectivity and reduce stimulation of neighbor muscles (van Elswijk et al., 2008; Neva et al., 2017). In addition, 20 single pulses were delivered to obtain a baseline response. The interval between pulses was randomized from 4 to 6 seconds. Pulse sequences were also randomized and divided into ten sessions of 62 pulses with a duration of about 5 min each, and with breaks of about 2 min. Coil temperature was monitored during the experiment using a thermal camera FLIR i3 (FLIR Systems, Wilsonville, OR, USA). If the temperature reached about 41 °C, stimulation was discontinued until the coil cooled down to about 32 °C.

#### 4.2.4 Data analysis

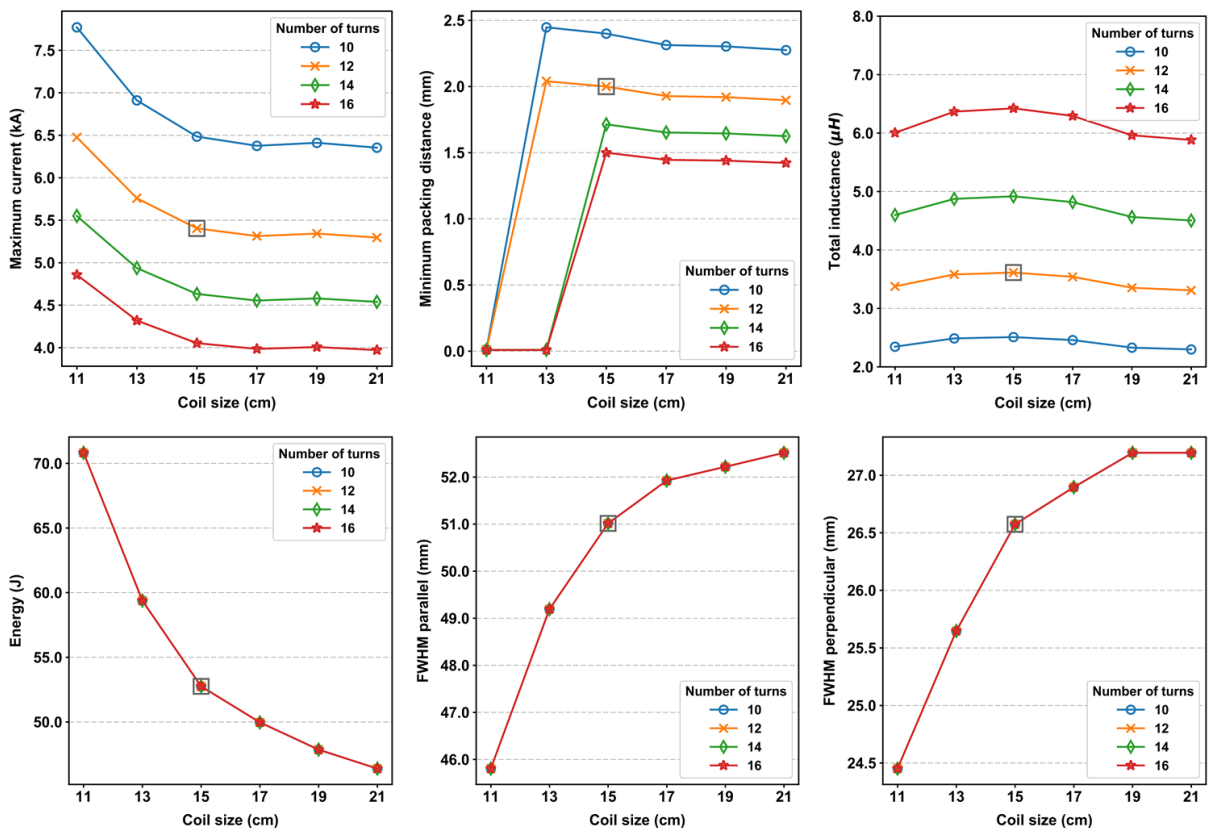
Data were analyzed using MATLAB R2013a (The MathWorks Inc.). Median MEP peak-to-peak amplitude and latency were computed for every orientation in each subject and normalized relative to the baseline values obtained with the orientation of 0°. MEPs with absolute amplitude lower than 50  $\mu\text{V}$  were excluded from the analysis. Across subjects, both amplitude and latency were averaged for each orientation. Then, a harmonics regression of sines and cosines was used to fit the curves of average MEP amplitude and latency, with degrees of 7 and 4, respectively. The FWHM and the anisotropy index (AI; Equation 4.2) were computed for each peak in the fitted curves (Kallioniemi et al., 2015a, 2015b). The AI ranges from 0 to 1, with values close to 1 suggesting that MEPs are generated after activating cortical neurons preferentially aligned in a narrow range of orientations.

$$\text{AI} = 1 - \frac{\text{FWHM}}{360^\circ} \quad (4.2)$$

## 4.3 Results

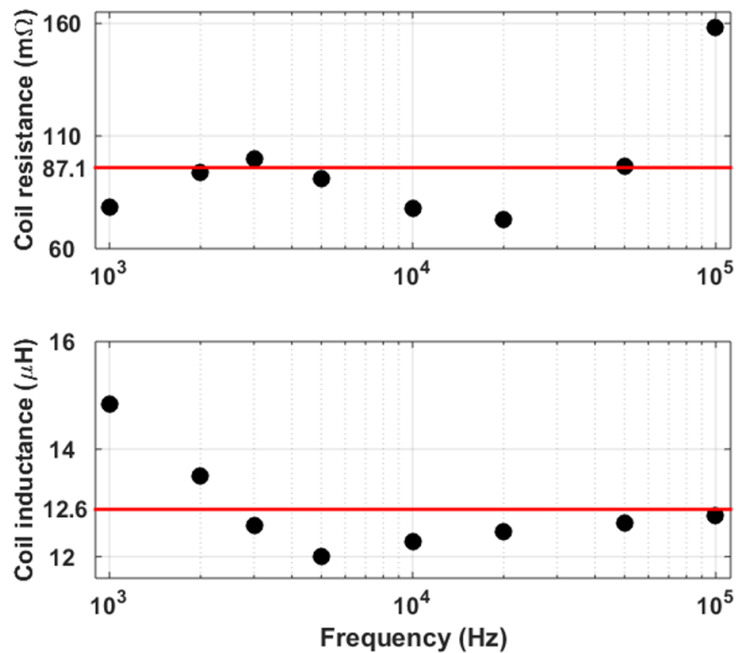
### 4.3.1 Coil optimization and validation

Figure 4.4 shows the results of optimization for maximum current required to generate a 100-V/m E-field in the spherical head surface, the total coil inductance, the minimum distance between innermost loops, energy, and FWHM components. The wire selected for coil manufacturing was 1.6-mm wide, making it impossible to consider 14 or 16 turns, as the minimum packing distance is lower than 1.7 mm. Also, the 10-turn models required more than 1 kA of additional current compared to the 12-turn models to induce the desired E-field, leading to the selection of the 12-turn models. Regarding the coil size, by increasing the diameter from 15 to 21 cm, there was no critical variation in required maximum current or inductance. However, the FWHM was about 2.5 mm higher in the parallel direction. Thus, we selected the coil model with a 15-cm diameter and 12 turns as the optimal solution for manufacturing.



**Figure 4.4:** Results obtained in the coil optimization procedure. Energy and E-field distribution were computed using the surface current distribution in the octagonal plane and were not affected by changing the number of loops. The gray square ( $\square$ ) highlights the coil model selected for production.

Next, we must consider the properties of the custom-made device used to apply the TMS pulses. Coil inductance should be between 10 to 20  $\mu\text{H}$ , and maximum required current below 3 kA, for practical use in human applications. By doubling the number of turns, the inductance is multiplied by a factor of 4 ( $L \propto N^2$ , where  $L$  is inductance and  $N$  the number of turns) and maximum current is halved ( $I_{\text{max}} \propto N$ , where  $I_{\text{max}}$  is maximum current). Therefore, to achieve the desired current and inductance, we manufactured each coil with two overlapping layers connected in series. Finally, the optimal solution was a set of two orthogonal coils, each with a 15-mm diameter and 24 turns allocated in two overlapping layers, i.e., 12 turns in each layer. With this model, the total coil inductance is 14.6  $\mu\text{H}$  and the minimum distance between inner loops 2 mm. Also, to generate a 100-V/m E-field, with FWHM parallel of 51.0 mm and perpendicular of 26.6 mm, the required current and energy are 2.7 kA and 52.5 J, respectively. Experimental measurements showed an average coil inductance of 12.6  $\mu\text{H}$  and the equivalent resistance of 87.1  $\text{m}\Omega$ , as shown in Figure 4.5.



**Figure 4.5:** Top and bottom graphs illustrate, respectively, the coil equivalent resistance and inductance measured for a range of sinusoidal waveforms with varying frequencies. Red solid lines represent the average value.

Estimated currents during the optimization procedure to generate an E-field in a specific orientation are shown in Figure 4.6A. Maximum current for the bottom coil is 20% lower than the required for the top coil. After experimental calibration, we obtained the equations that give

the capacitor voltage in Volts necessary to generate an E-field with norm  $|E|$  given in V/m at an orientation  $\theta$ :

$$V_{\text{bottom}}(|E|, \theta) = (8.6838) \cdot |E| \cos \theta \quad (4.3)$$

$$V_{\text{top}}(|E|, \theta) = (11.2751) \cdot |E| \sin \theta \quad (4.4)$$

The capacitor voltage to induce a 100-V/m E-field with the bottom coil was 868 V; for the top coil, it was 1120 V. The bottom coil required 22.5% less voltage than the top coil. This value differed only 2.5% from the estimate for the current during optimization. The average deviations from theoretical values in E-field norm and orientation ( $\Delta E$  and  $\Delta \theta$ ) for stimulation with 25 V/m and orientation from 0 to 180° were 0.1 V/m and 1.3°, respectively (Figure 4.6B).

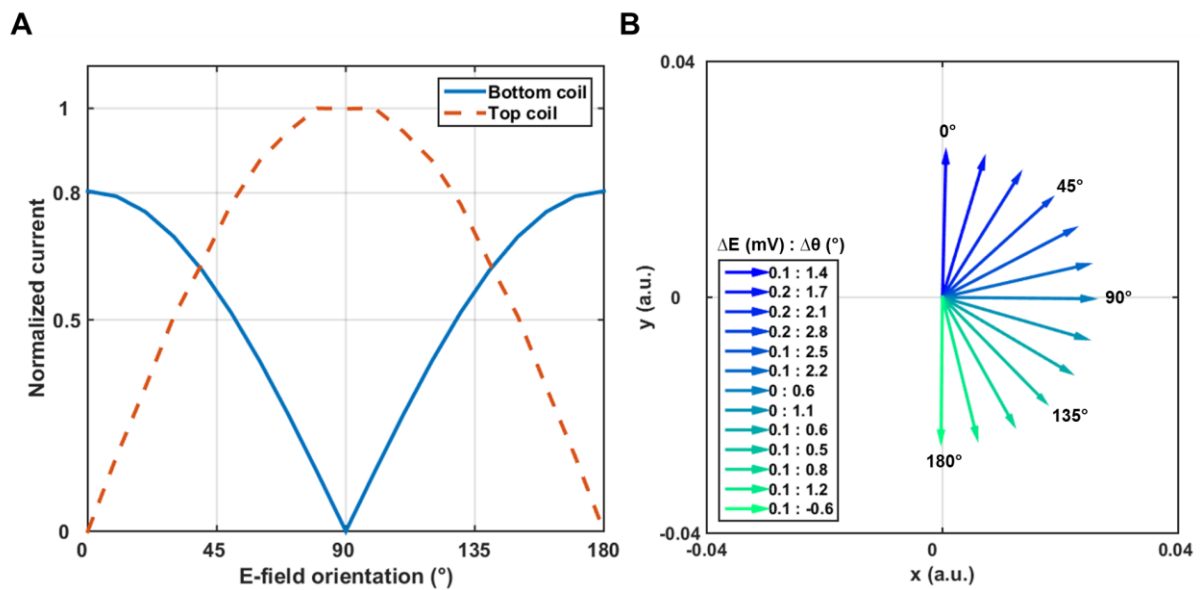


**Figure 4.6:** **A)** Estimated normalized current required to induce an E-field in each orientation for the top (dashed line) and bottom (solid line) coils. **B)** E-field norm and orientation measured with the probe shown in Figure 4.3B. E-field was set to 25 V/m, and orientation varied from 0 to 180° in steps of 15°. The inserted box shows the differences between the set E-field ( $\Delta E$ ) and orientation ( $\Delta \theta$ ) values and measured values.

The E-field distribution with the orientation set to 0, 45 and 90°, measured over a hemispherical surface are illustrated in Figure 4.7. The FWHM profile of E-field in parallel and perpendicular directions for the top and bottom coils are shown in Figure 4.7A. Perpendicular FWHM of the bottom and top coils were 25.6 and 26.5 mm, respectively. Parallel FWHM was 44.8 and 46.4 mm for the bottom and top coils, respectively.

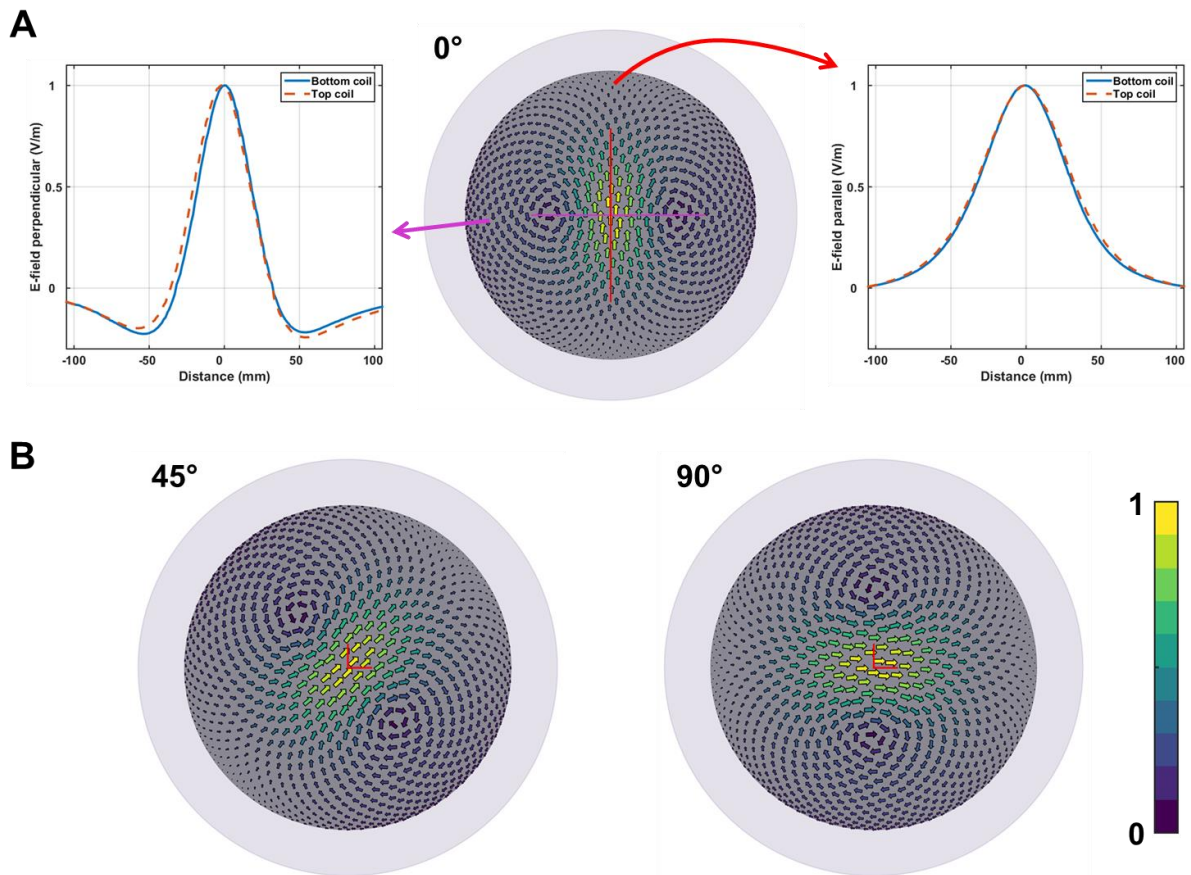


**Figure 4.7:** **A)** Left and right plots show the normalized E-field profile in perpendicular (pink arrow) and parallel (red arrow) orientations, respectively. The central plot illustrates the induced E-field distribution in the spherical cortical surface with 70-mm radius for a TMS pulse at 0°. The shaded gray outer sphere represents the spherical scalp with an 85-mm radius. **B)** Vector plots of TMS induced E-fields at 45 and 90°. Color scale represents the normalized E-field norm.

### 4.3.2 Motor cortex orientation-dependency

Relative MEP amplitudes showed two peaks, the highest at 0° and a lower one at 180°. Both peaks were oriented approximately perpendicular to the central sulcus, but with current flowing in opposite directions. The AI was 0.84 and 0.87 for the 0 and 180° peak, respectively. FWHM was 57.5 and 47.8 mm for these peaks, respectively. The MEP amplitudes were reduced to almost zero for the entire quadrants between 45 – 135° and 225 – 315°. MEPs showed lowest latencies for angles near 0 and 180°, of about 23 ms, and highest latencies for angles near 90 and 270°, of about 24 ms. Polar plots of the harmonics fit are shown in Figure 4.8.

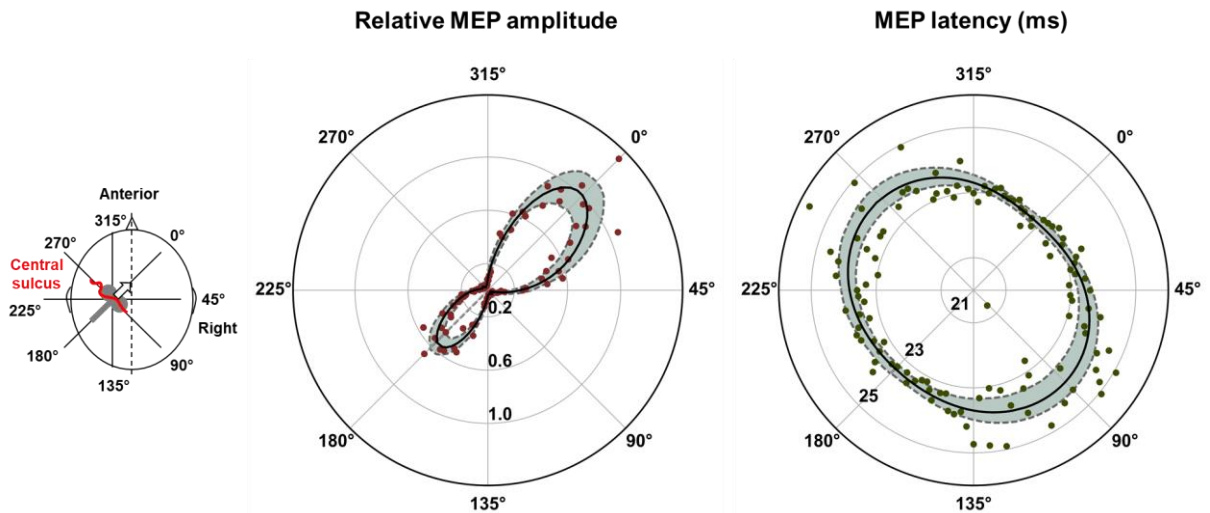


**Figure 4.8:** Polar plots of average relative MEP amplitude and latency for each orientation of stimulus. The solid black line represents the harmonics fit and shaded area limited by the dashed line stands for the error of the fit. Each red or green dot represents the average relative MEP amplitude or latency across all subjects for a specific orientation, respectively. In the left, a schematic representation of the reference for defining the stimulus orientation is shown.  $0^\circ$  was the orientation in which the hotspot and motor threshold was measured, approximately perpendicular to the central sulcus.

## 4.4 Discussion

In this study, we developed a mTMS coil to control the E-field orientation electronically and investigated the orientation-dependency of the primary motor cortex. The procedure for optimization of minimum-energy coils allowed the successful construction and calibration of the mTMS coil with rotating E-field. Also, assessing MEPs with high-angular resolution revealed consistent high amplitude around  $45^\circ$  and  $135^\circ$ , followed by the lowest MEPs latencies. The novel mTMS might allow further studies to apply stimulation in different orientations without the need for mechanical adjustment of the coil.

### 4.4.1 Developed mTMS coil

The developed mTMS coil is energy-efficient and allows one to change the induced E-field orientation by adjusting the current applied to each of the two overlapping coils. The top coil required 30% more capacitor charge than the bottom coil, to generate a given E-field. This difference is due to the 5-mm extra distance of the top coil from the cortical surface. In fact, the increase in distance directly requires higher stimulation currents because of a worse coil-cortex coupling (Koponen et al., 2017), and is a limiting factor for manufacturing overlapping coils.

The top coil also has slightly lower focality than the bottom coil, i.e., larger FWHM of induced E-field. However, the increase in perpendicular and parallel directions of 0.9 and 1.6 mm accounts for about 3% of change and might be negligible for the current application.

The energy and current required for a 100-V/m in 0° orientation are lower than those previously reported. The conventional coil requires 6.4 kA and 330 J to induce a 100-V/m E-field (Koponen et al., 2015), while the developed coil needs 2.7 kA and 52.5 J. Required current is not directly comparable between both coils, as the inductance of the conventional coil is about 3.3  $\mu$ H higher. However, the considerably lower energy allows the developed coil to apply a higher number of pulses without heating up to undesired temperatures. The relatively low required current in our coil corresponds to a lower capacitor voltage. Thus, the time needed to recharge the capacitors is also shortened, making it easier to design electronics for fast pulse sequences. For instance, shorter interval between stimuli is of great importance in studies of short-interval cortical inhibition and facilitation, with paired-pulse TMS (Delvendahl et al., 2014; Rossini et al., 2015). In this case, two consecutive pulses are applied within a millisecond interval, benefiting from the smaller current requirement.

The previous minimum-energy coil design introduced by Koponen et al. (2017) has an inductance of 9  $\mu$ H, maximum energy of 40 J and requires 570 V to induce a 100-V/m E-field. Our coil (bottom coil) requires a higher voltage (868 V) and energy (52.5 J) but also has a higher inductance (12.6  $\mu$ H). For this study, the considerably higher voltage was not a limiting factor, thanks to the available stimulator electronics. The higher inductance was achieved by doubling the number of turns distributed in two layers. In addition, the inductance obtained led to a required maximum current similar to that of the previous minimum-energy coil. It is important to note that every additional layer of winding causes the top-most overlapped coils to be even more distant from the cortical surface. Thus, the compromise between required current, inductance and desired focality must be considered while designing a mTMS coil (Deng et al., 2013; Koponen et al., 2017).

The diameter of the developed coil is similar to that of the conventional Magstim 70 mm Double Coil, and almost half of the length of previously manufactured minimum-energy coil (Koponen et al., 2017). The compact design contributes to more comfortable positioning over the scalp, and better handling during long experiments, even when guided with navigation systems. The glass-filled polyamide seems to be resistant to the Lorentz force during the TMS pulse. Also, the possibility to use 3D-printed materials might ease the manufacturing of coils with more complicated patterns of coil windings, such as those reported by Deng et al. (2008).

#### 4.4.2 Motor cortex orientation-dependency

The literature has a wide variety of definitions for the angular reference system used to position the TMS coil. Therefore, we must describe ours for better readership and understanding. We defined for each subject the  $0^\circ$  (posterior-anterior direction) as the orientation that elicited highest MEPs during hotspot and motor-threshold search, like recent studies (Bashir et al., 2013; D'Ostilio et al., 2016; Kallioniemi et al., 2015a). Earlier reports assumed the  $0^\circ$  (posterior-anterior) as the orientation parallel, and  $90^\circ$  (lateral-medial) perpendicular to the midsagittal line (Brasil-Neto et al., 1992; Di Lazzaro et al., 2008; Souza et al., 2017; Werhahn et al., 1994). For comparison, the  $0^\circ$  of earlier studies corresponds to our  $315^\circ$ , and  $90^\circ$  to our  $45^\circ$ . Soon, the use of neuronavigation is expected to become widely spread. Most of TMS groups will be able to follow the central sulcus as a reference for coil placement. To our understanding, defining a standard reference would allow more straightforward comparison of results across studies, and the  $0^\circ$  as used in our study seems to be a good candidate.

MEP amplitudes followed by lowest MEP latencies were observed for the E-field aligned approximately perpendicular to the central sulcus. Also, E-field aligned parallel to the central sulcus, i.e.,  $90$  and  $270^\circ$ , consistently elicited MEPs with relatively low amplitude and longer latencies by about 1 ms. Regarding MEP amplitudes, our results are in accordance with previous studies (Kallioniemi et al., 2015a; Souza et al., 2017). Stimulation at steps of  $3^\circ$  allowed a smooth estimation of MEP amplitudes across all possible orientations. Furthermore, the harmonics regression seems to provide a similar distribution than the Gaussian fit applied for the highest peak by Kallioniemi et al. (2015). We estimated the AI not only for the highest MEP amplitudes at the posterior-anterior direction but also for the anterior-posterior orientation. AI in both curves was almost the same. This observation suggests that even with non-optimal functional activation at the anterior-posterior direction, i.e., lower MEP amplitudes, the estimated level of anisotropy is maintained. In this case, AI would possibly be associated with the structural alignment of underlying cortical neurons (Kallioniemi et al., 2015a, 2015b). Therefore, our results support AI as a putative TMS marker for structural assessment of motor cortex.

Surprisingly, MEP latencies varied differently than previously reported. Lowest latencies were observed for the E-field aligned approximately perpendicular to the central sulcus, whereas E-field aligned parallel to the central sulcus evoked MEPs with about 1-ms longer latencies. It has been shown that current flowing in lateral-medial direction is more likely to

activate the axons of neurons, and thus generate earlier MEPs (Di Lazzaro et al., 2001; Werhahn et al., 1994). However, lower latencies at posterior-anterior and anterior-posterior directions suggest that activation of axons might occur preferentially with E-field aligned parallel to neuronal bundles at bending ends, which is supported by early simulation studies (Abdeen and Stuchly, 1994). It is important to note that most studies that investigated MEP latencies defined lateral-medial and posterior-anterior directions relative to the midsagittal line, represented by 315 and 45° in this study, respectively. These are transitional orientations, and small deviations in any direction might lead to distinct alignments relative to the neuronal bundles. Most importantly, those studies did not use any neuronavigation system for stable coil positioning relative to anatomical structures. For instance, Figure 4.8 shows that at 45° a shift towards the back of the head would evoke MEPs with lower amplitudes and higher latencies (perpendicular alignment with neurons). In turn, a shift towards the anterior direction would elicit MEPs with higher latencies and lower amplitudes (parallel alignment with neurons). The studied transitional orientation also possibly accounts for the increased variability in measured MEP parameters. Despite the different results, we observed MEP latencies higher for anterior-posterior compared to posterior-anterior, as previously detected. This latter increase in latency is most likely explained by the activation of different circuits with distinct synaptic inputs (D'Ostilio et al., 2016; Hannah and Rothwell, 2017). Thus, compared to posterior-anterior, the E-field in anterior-posterior direction possibly activates other neural populations with distinct mechanisms and synchronization patterns.

Finally, it is essential to highlight the limitations and advantages of our findings. First, pulses were applied with a 60- $\mu$ s monophasic current, which tends to elicit more consistent MEPs across different orientations (D'Ostilio et al., 2016; Di Lazzaro et al., 2008). Second, no statistical analysis was performed to compare MEP amplitudes and latencies between different orientations. Therefore, our observations were based on visual graph analysis, and future analysis should explore the statistical significance. Nevertheless, the errors associated with the curve fitting were estimated and might evidence possible differences. Third, the study was performed without any mechanical movement of the stimulation coil and with the aid of neuronavigation. Different from all previous studies, the stimuli were applied with electronic control of the E-field orientation and provided highly stable coil positioning. In this case, the errors associated to holding the coil tangential to the scalp and adjusting the correct orientation are solely due to the errors of navigation tracking (3 mm; 3°) and to adjust the E-field orientation (about 1.3°). Fourth and last, the electronic control of E-field orientation opens the possibility for new paradigms regarding TMS protocols. By combining techniques of image processing in

neuronavigation with the stimulation device, it might be possible to automatically adjust the E-field orientation relative to a preselected cortical area. Also, paired-pulse protocols might benefit from changing the orientation of the E-field within a millisecond interval without the need of mechanical movement of the coil. The later would allow to further study the orientation-dependency of mechanisms in short-interval inhibition and facilitation (Delvendahl et al., 2014; Ziemann et al., 1996).

## **4.5 Conclusion**

The electronic control of E-field orientation seems to be a breakthrough step in the study of cortical stimulation and opens the possibility for new technologies regarding TMS protocols. For instance, paired-pulse protocols might benefit from changing the orientation of the E-field within a millisecond interval without the need of mechanical movement of the coil. The later would allow to further study the orientation-dependency of mechanisms in short-interval inhibition and facilitation (Delvendahl et al., 2014; Ziemann et al., 1996). By combining techniques of image processing in neuronavigation with the stimulation device, it might be possible to automatically adjust the E-field orientation relative to a preselected cortical area and therefore achieve better accuracy and reliability for TMS.

## 5. Final remarks

---

This thesis presents new methods for improving the accuracy of brain interventions procedures that are relatively new and still under development. The developed InVesalius Navigator software is a low-cost neuronavigation system and might bring the technology of image-guided positioning closer to research centers with limited resources. The accuracy and reliability of the algorithm are similar to commercial systems and has the advantage of unique features for image processing, compatibility with multiple tracking devices and instrument positioning, such as a TMS coil. Moreover, the combined use of InVesalius Navigator with 3D-printed patient-specific models might be useful to aid the medical team in practicing and planning neurosurgeries. Finally, the new manufactured mTMS coil allows electronic control of the stimulus orientation with high angular resolution. Such a device might open new possibilities to study mechanisms of brain function and provide better accuracy in targeting cortical brain structures.

In the future, we plan to implement a series of new features to InVesalius Navigator. For instance, improved compatibility with a larger number of tracking devices, better tools for MRI brain segmentation, and computation of E-field distribution during navigated TMS. In addition, the mTMS technology seems to be a breakthrough in the field, and much research is still to be done in developing other coils to allow not only the electronic control of stimulus orientation but also the position. Finally, we plan to further improve the accuracy and reliability of TMS by integrating the image-guidance of neuronavigation with the electronic control of TMS pulses, and thus, enable individualized stimulation relative to subject's anatomy.

Lastly, it is important to state that studies on technological development are of utmost importance to provide new tools to understand and investigate the most complex structure of the human body, the brain.

## 6. References

---

- Abdeen MA, Stuchly MA. Modeling of magnetic field stimulation of bent neurons. *IEEE Trans Biomed Eng* 1994;41:1092–5. doi:10.1109/10.335848.
- Ambrosini E, Ferrante S, van de Ruit M, Biguzzi S, Colombo V, Monticone M, et al. StimTrack: An open-source software for manual transcranial magnetic stimulation coil positioning. *J Neurosci Methods* 2018;293:97–104. doi:10.1016/j.jneumeth.2017.09.012.
- Amorim P, Moraes T, Silva J, Pedrini H. InVesalius: An Interactive Rendering Framework for Health Care Support. In: Bebis G, Boyle R, Parvin B, Koracin D, Pavlidis I, Feris R, et al., editors. *Adv. Vis. Comput. 11th Int. Symp. ISVC 2015, Las Vegas, NV, USA, December 14–16, 2015, Proceedings, Part I*, Cham, Switzerland: Springer International Publishing; 2015, p. 45–54. doi:10.1007/978-3-319-27857-5\_5.
- Barker AT, Jalinous R, Freeston IL. Non-invasive magnetic stimulation of human motor cortex. *Lancet* 1985;1:1106–7. doi:10.1016/S0140-6736(85)92413-4.
- Bashir S, Perez JM, Horvath JC, Pascual-Leone A. Differentiation of motor cortical representation of hand muscles by navigated mapping of optimal TMS current directions in healthy subjects. *J Clin Neurophysiol* 2013;30:390–5. doi:10.1097/WNP.0b013e31829dda6b.
- Brasil-Neto JP, Cohen LG, Panizza M, Nilsson J, Roth BJ, Hallett M. Optimal focal transcranial magnetic activation of the human motor cortex: effects of coil orientation, shape of the induced current pulse, and stimulus intensity. *J Clin Neurophysiol* 1992;9:132–6. doi:10.1097/00004691-199201000-00014.
- Chiarelli AM, Maclin EL, Low K a., Fabiani M, Gratton G. Comparison of procedures for co-registering scalp-recording locations to anatomical magnetic resonance images. *J Biomed Opt* 2015;20:16009. doi:10.1117/1.JBO.20.1.016009.
- Choi J-Y, Choi J-H, Kim N-K, Kim Y, Lee J-K, Kim M-K, et al. Analysis of errors in medical rapid prototyping models. *Int J Oral Maxillofac Surg* 2002;31:23–32. doi:10.1054/ijom.2000.0135.
- Clarkson MJ, Zombori G, Thompson S, Totz J, Song Y, Espak M, et al. The NifTK software platform for image-guided interventions: platform overview and NiftyLink messaging. *Int J Comput Assist Radiol Surg* 2015;10:301–16. doi:10.1007/s11548-014-1124-7.
- Cooper JB, Taqueti VR. A brief history of the development of mannequin simulators for clinical education and training. *Postgrad Med J* 2008;84:563–70. doi:10.1136/qshc.2004.009886.
- D’Ostilio K, Goetz SM, Hannah R, Ciocca M, Chieffo R, Chen JA, et al. Effect of coil orientation on strength-duration time constant and I-wave activation with controllable pulse parameter transcranial magnetic stimulation. *Clin Neurophysiol* 2016;127:675–83. doi:10.1016/j.clinph.2015.05.017.
- Delvendahl I, Lindemann H, Jung NH, Pechmann A, Siebner HR, Mall V. Influence of Waveform and Current Direction on Short-Interval Intracortical Facilitation: A Paired-Pulse

TMS Study. *Brain Stimul* 2014;7:49–58. doi:10.1016/j.brs.2013.08.002.

Deng Z-D, Lisanby SH, Peterchev A V. Electric field depth-focality tradeoff in transcranial magnetic stimulation: simulation comparison of 50 coil designs. *Brain Stimul* 2013;6:1–13. doi:10.1016/j.brs.2012.02.005.

Deng Z, Peterchev A V, Lisanby SH. Coil design considerations for deep-brain transcranial magnetic stimulation (dTMS). *Conf. Proc. Annu. Int. Conf. IEEE Eng. Med. Biol. Soc. IEEE Eng. Med. Biol. Soc.*, vol. 2008, 2008, p. 5675–9. doi:10.1109/IEMBS.2008.4650502.

van Elswijk G, Kleine BU, Overeem S, Eshuis B, Hekkert KD, Stegeman DF. Muscle imaging: mapping responses to transcranial magnetic stimulation with high-density surface electromyography. *Cortex* 2008;44:609–16. doi:10.1016/j.cortex.2007.07.003.

Fedorov A, Beichel R, Kalpathy-Cramer J, Finet J, Fillion-Robin J-C, Pujol S, et al. 3D Slicer as an image computing platform for the Quantitative Imaging Network. *Magn Reson Imaging* 2012;30:1323–41. doi:10.1016/j.mri.2012.05.001.

Filho FVG, Coelho G, Cavalheiro S, Lyra M, Zymberg ST. Quality assessment of a new surgical simulator for neuroendoscopic training. *Neurosurg Focus* 2011;30:E17. doi:10.3171/2011.2.FOCUS10321.

Fitzpatrick JM, West JB, Maurer CR. Predicting error in rigid-body point-based registration. *IEEE Trans Med Imaging* 1998;17:694–702. doi:10.1109/42.736021.

Garcia MAC, Souza VH, Vargas CD. Can the Recording of Motor Potentials Evoked by Transcranial Magnetic Stimulation Be Optimized? *Front Hum Neurosci* 2017;11. doi:10.3389/fnhum.2017.00413.

Gasco J, Holbrook TJ, Patel A, Smith A, Paulson D, Muns A, et al. Neurosurgery Simulation in Residency Training. *Neurosurgery* 2013;73:S39–45. doi:10.1227/NEU.0000000000000102.

Gramfort A. MEG and EEG data analysis with MNE-Python. *Front Neurosci* 2013;7. doi:10.3389/fnins.2013.00267.

Grillo FW, Souza VH, Matsuda RH, Rondinoni C, Pavan TZ, Baffa O, et al. Patient-specific neurosurgical phantom: assessment of visual quality, accuracy, and scaling effects. *3D Print Med* 2018;4:3. doi:10.1186/s41205-018-0025-8.

Hallett M. Transcranial magnetic stimulation and the human brain. *Nature* 2000;406:147–50. doi:10.1038/35018000.

Hannah R, Rothwell JC. Pulse Duration as Well as Current Direction Determines the Specificity of Transcranial Magnetic Stimulation of Motor Cortex during Contraction. *Brain Stimul* 2017;10:106–15. doi:10.1016/j.brs.2016.09.008.

Horn BKP. Closed-form solution of absolute orientation using unit quaternions. *J Opt Soc Am A* 1987;4:629. doi:10.1364/JOSAA.4.000629.

Julkunen P. Methods for estimating cortical motor representation size and location in navigated transcranial magnetic stimulation. *J Neurosci Methods* 2014;232:125–33.

## References

doi:10.1016/j.jneumeth.2014.05.020.

Kallioniemi E, Könönen M, Julkunen P. Repeatability of functional anisotropy in navigated transcranial magnetic stimulation – coil-orientation versus response. *Neuroreport* 2015a;26:515–21. doi:10.1097/WNR.0000000000000380.

Kallioniemi E, Könönen M, Säisänen L, Gröhn H, Julkunen P. Functional neuronal anisotropy assessed with neuronavigated transcranial magnetic stimulation. *J Neurosci Methods* 2015b;256:82–90. doi:10.1016/j.jneumeth.2015.08.028.

Koponen LM. Large thin overlapping coils, a novel approach for multichannel transcranial magnetic stimulation. Aalto University, 2013.

Koponen LM, Nieminen JO, Ilmoniemi RJ. Minimum-energy Coils for Transcranial Magnetic Stimulation: Application to Focal Stimulation. *Brain Stimul* 2015;8:124–34. doi:10.1016/j.brs.2014.10.002.

Koponen LM, Nieminen JO, Mutanen TP, Stenroos M, Ilmoniemi RJ. Coil optimisation for transcranial magnetic stimulation in realistic head geometry. *Brain Stimul* 2017;10:795–805. doi:10.1016/j.brs.2017.04.001.

Kuehn B, Mularski S, Schoenherr S, Hammersen S, Stendel R, Kombos T, et al. Sensor-based neuronavigation: Evaluation of a large continuous patient population. *Clin Neurol Neurosurg* 2008;110:1012–9. doi:10.1016/j.clineuro.2008.06.017.

Di Lazzaro V, Oliviero a., Saturno E, Pilato F, Insola a., Mazzone P, et al. The effect on corticospinal volleys of reversing the direction of current induced in the motor cortex by transcranial magnetic stimulation. *Exp Brain Res* 2001;138:268–73. doi:10.1007/s002210100722.

Di Lazzaro V, Ziemann U, Lemon RN. State of the art: Physiology of transcranial motor cortex stimulation. *Brain Stimul* 2008;1:345–62. doi:10.1016/j.brs.2008.07.004.

Little G, Boe S, Bardouille T. Head movement compensation in real-time magnetoencephalographic recordings. *MethodsX* 2014;1:275–82. doi:10.1016/j.mex.2014.10.008.

Maciunas RJ, Galloway Jr. RL, Latimer J, Cobb C, Zaccharias E, Moore A, et al. An Independent Application Accuracy Evaluation of Stereotactic Frame Systems. *Stereotact Funct Neurosurg* 1992;58:103–7. doi:10.1159/000098981.

Mascott CR. In vivo accuracy of image guidance performed using optical tracking and optimized registration. *J Neurosurg* 2006;105:561–7. doi:10.3171/jns.2006.105.4.561.

McNair NA. MagPy: A Python toolbox for controlling Magstim transcranial magnetic stimulators. *J Neurosci Methods* 2017;276:33–7. doi:10.1016/j.jneumeth.2016.11.006.

Neggers SFW, Petrov PI, Mandija S, Sommer IEC, van den Berg NAT. Understanding the biophysical effects of transcranial magnetic stimulation on brain tissue, 2015, p. 229–59. doi:10.1016/bs.pbr.2015.06.015.

Neva JL, Gallina A, Peters S, Garland SJ, Boyd LA. Differentiation of motor evoked

## References

potentials elicited from multiple forearm muscles: An investigation with high-density surface electromyography. *Brain Res* 2017;1676:91–9. doi:10.1016/j.brainres.2017.09.017.

Nieminen JO, Koponen LM, Ilmoniemi RJ. Experimental Characterization of the Electric Field Distribution Induced by TMS Devices. *Brain Stimul* 2015:1–8. doi:10.1016/j.brs.2015.01.004.

Nolden M, Zelzer S, Seitel A, Wald D, Müller M, Franz AM, et al. The Medical Imaging Interaction Toolkit: challenges and advances. *Int J Comput Assist Radiol Surg* 2013;8:607–20. doi:10.1007/s11548-013-0840-8.

Nummenmaa A, Stenroos M, Ilmoniemi RJ, Okada YC, Hämäläinen MS, Raij T. Comparison of spherical and realistically shaped boundary element head models for transcranial magnetic stimulation navigation. *Clin Neurophysiol* 2013;124:1995–2007. doi:10.1016/j.clinph.2013.04.019.

Och JG, Clarcke GD, Sobol WT, Rosen CW, Mun SK. Acceptance testing of magnetic resonance imaging systems: Report of AAPM Nuclear Magnetic Resonance Task Group No. 6. *Med Phys* 1992;19:217. doi:10.1118/1.596903.

Omara AI, Wang M, Fan Y, Song Z. Anatomical landmarks for point-matching registration in image-guided neurosurgery. *Int J Med Robot Comput Assist Surg* 2014;10:55–64. doi:10.1002/rcs.1509.

Orringer D a, Golby A, Jolesz F. Neuronavigation in the surgical management of brain tumors: current and future trends. *Expert Rev Med Devices* 2012;9:491–500. doi:10.1586/erd.12.42.

Peirce JW. PsychoPy—Psychophysics software in Python. *J Neurosci Methods* 2007;162:8–13. doi:10.1016/j.jneumeth.2006.11.017.

Peres ASC, Souza VH, Catunda JMY, Mazzeto-Betti KC, Santos-Pontelli TEG, Vargas CD, et al. Can somatosensory electrical stimulation relieve spasticity in post-stroke patients? A TMS pilot study. *Biomed Eng / Biomed Tech* 2017. doi:10.1515/bmt-2016-0162.

Peres ASC, Souza VHO, Maziero D, de Araujo DB, Salmon CEG, Baffa O. Vector magnetic field mapping of a Transcranial Magnetic Stimulation coil using Magnetic Resonance Imaging: in vitro and in vivo experiments. *IFMBE Proc.*, vol. 25. 7th ed., 2009, p. 571–4. doi:10.1007/978-3-642-03885-3\_159.

Peterchev A V, D’Ostilio K, Rothwell JC, Murphy DL. Controllable pulse parameter transcranial magnetic stimulator with enhanced circuit topology and pulse shaping. *J Neural Eng* 2014;11:56023. doi:10.1088/1741-2560/11/5/056023.

Poggi S, Pallotta S, Russo S, Gallina P, Torresin A, Bucciolini M. Neuronavigation accuracy dependence on CT and MR imaging parameters: a phantom-based study. *Phys Med Biol* 2003;48:2199–216. doi:10.1088/0031-9155/48/14/311.

Rondinoni C, Souza VHO, Matsuda RH, Salles ACP, Santos MV, Filho OB, et al. Inter-institutional protocol describing the use of three-dimensional printing for surgical planning in a patient with childhood epilepsy: From 3D modeling to neuronavigation. 2014 IEEE 16th

## References

Int. Conf. e-Health Networking, Appl. Serv., 2014, p. 347–9.  
doi:10.1109/HealthCom.2014.7001866.

Rossini PM, Burke D, Chen R, Cohen LG, Daskalakis Z, Di Iorio R, et al. Non-invasive electrical and magnetic stimulation of the brain, spinal cord, roots and peripheral nerves: Basic principles and procedures for routine clinical and research application. An updated report from an I.F.C.N. Committee. *Clin Neurophysiol* 2015;126:1071–107.  
doi:10.1016/j.clinph.2015.02.001.

Ruohonen J, Ilmoniemi RJ. Focusing and targeting of magnetic brain stimulation using multiple coils. *Med Biol Eng Comput* 1998;36:297–301. doi:10.1007/BF02522474.

Ruohonen J, Karhu J. Navigated transcranial magnetic stimulation. *Neurophysiol Clin* 2010;40:7–17. doi:10.1016/j.neucli.2010.01.006.

Ruohonen J, Ravazzani P, Grandori F, Ilmoniemi RJ. Theory of multichannel magnetic stimulation: toward functional neuromuscular rehabilitation. *IEEE Trans Biomed Eng* 1999;46:646–51. doi:10.1109/10.764941.

Souza VH, Vieira TM, Peres ASC, Garcia MAC, Vargas CD, Baffa O. Effect of TMS coil orientation on the spatial distribution of motor evoked potentials in an intrinsic hand muscle. *Biomed Eng / Biomed Tech* 2017. doi:10.1515/bmt-2016-0240.

Steinmeier R, Rachinger J, Kaus M, Ganslandt O, Huk W, Fahlbusch R. Factors influencing the application accuracy of neuronavigation systems. *Stereotact Funct Neurosurg* 2000;75:188–202. doi:10.1159/000048404.

Thielscher A, Kammer T. Linking physics with physiology in TMS: a sphere field model to determine the cortical stimulation site in TMS. *Neuroimage* 2002;17:1117–30.  
doi:10.1006/nimg.2002.1282.

Tsuzuki D, Dan I. Spatial registration for functional near-infrared spectroscopy: from channel position on the scalp to cortical location in individual and group analyses. *Neuroimage* 2014;85 Pt 1:92–103. doi:10.1016/j.neuroimage.2013.07.025.

Ueno S, Tashiro T, Harada K. Localized stimulation of neural tissues in the brain by means of a paired configuration of time-varying magnetic fields. *J Appl Phys* 1988;64:5862–4.  
doi:10.1063/1.342181.

Vannier MW, Marsh JL, Warren JO. Three dimensional CT reconstruction images for craniofacial surgical planning and evaluation. *Radiology* 1984;150:179–84.  
doi:10.1148/radiology.150.1.6689758.

Wassermann E, Epstein C, Ziemann U, editors. *The Oxford handbook of transcranial stimulation*. Oxford University Press; 2012. doi:10.1093/oxfordhb/9780198568926.001.0001.

Wassermann EM, McShane LM, Hallett M, Cohen LG. Noninvasive mapping of muscle representations in human motor cortex. *Electroencephalogr Clin Neurophysiol* 1992;85:1–8.  
doi:10.1016/0168-5597(92)90094-R.

Wassermann EM, Zimmermann T. Transcranial magnetic brain stimulation: Therapeutic

## References

promises and scientific gaps. *Pharmacol Ther* 2012;133:98–107.  
doi:10.1016/j.pharmthera.2011.09.003.

Werhahn KJ, Fong JK, Meyer BU, Priori A, Rothwell JC, Day BL, et al. The effect of magnetic coil orientation on the latency of surface EMG and single motor unit responses in the first dorsal interosseous muscle. *Electroencephalogr Clin Neurophysiol* 1994;93:138–46.  
doi:10.1016/0168-5597(94)90077-9.

Wu C-T, Lee S-T, Chen J-F, Lin K-L, Yen S-H. Computer-Aided Design for Three-Dimensional Titanium Mesh Used for Repairing Skull Base Bone Defect in Pediatric Neurofibromatosis Type 1. *Pediatr Neurosurg* 2008;44:133–9. doi:10.1159/000113116.

Ziemann U. Transcranial Magnetic Stimulation: Its Current Role in the Evaluation of Patients Post-Stroke. *J Neurol Phys Ther* 2000;24:82–93.

Ziemann U, Rothwell JC, Ridding MC. Interaction between intracortical inhibition and facilitation in human motor cortex. *J Physiol* 1996;496:873–81.  
doi:10.1113/jphysiol.1996.sp021734.

# Appendix A

---

Consider a coordinate system E that belongs to  $\mathbb{R}^3$ . The aim is to find the change of basis matrix from the canonical reference system  $\mathbb{R}^3$  to E. To do so, first we need to collect three distinct points,  $P_1$ ,  $P_2$  and  $P_3$  with coordinates given in  $\mathbb{R}^3$ . Then, a vector  $\mathbf{v}_1^{\text{aux}}$  is created subtracting  $P_2$  from  $P_1$ . A second vector  $\mathbf{v}_2^{\text{aux}}$  is created subtracting  $P_3$  from  $P_1$ . The point resulting from the projection of  $\mathbf{v}_2^{\text{aux}}$  in  $\mathbf{v}_1^{\text{aux}}$  will be used as the origin Q. Then, vector  $\mathbf{v}_1$  is computed from  $P_3$  to Q and  $\mathbf{v}_2$  is computed from  $P_1$  to Q. Vector  $\mathbf{v}_3$  is obtained by the cross product between  $\mathbf{v}_1$  and  $\mathbf{v}_2$ . Then, we define the correspondent transformation matrix of E.

$$\mathbf{v}_1 = \frac{P_1 - Q}{|P_1 - Q|} \quad (\text{A.1})$$

$$\mathbf{v}_2 = \frac{P_2 - Q}{|P_2 - Q|} \quad (\text{A.2})$$

$$\mathbf{v}_3 = \mathbf{v}_1 \times \mathbf{v}_2 \quad (\text{A.3})$$

$$M = \begin{bmatrix} v_{1,1} & v_{2,1} & v_{3,1} \\ v_{1,2} & v_{2,2} & v_{3,2} \\ v_{1,3} & v_{2,3} & v_{3,3} \end{bmatrix} \quad (\text{A.4})$$

